A&A 665, A105 (2022)
https://doi.org/10.1051/0004-6361/202142367

Astronomy & Astrophysics

Galaxy populations in the Hydra I cluster from the VEGAS survey

II. The ultra-diffuse galaxy population

Antonio La Marca[1,2,3], Enrichetta Iodice[1], Michele Cantiello[4], Duncan A. Forbes[5], Marina Rejkuba[6], Michael Hilker[6], Magda Arnaboldi[6], Laura Greggio[7], Chiara Spiniello[1,9], Steffen Mieske[10], Aku Venhola[11], Marilena Spavone[1], Giuseppe D'Ago[12], Maria Angela Raj[13], Rossella Ragusa[1,3], Marco Mirabile[3], Roberto Rampazzo[8], Reynier Peletier[2], Maurizio Paolillo[1,3], Nelvy Choque Challapa[2], and Pietro Schipani[1]

[1] INAF – Astronomical Observatory of Capodimonte, Salita Moiariello 16, 80131 Naples, Italy
e-mail: antoniolamarca46@gmail.com
[2] Kapteyn Institute, University of Groningen, Landleven 12, 9747 AD Groningen, The Netherlands
[3] University of Naples "Federico II", C.U. Monte Sant'Angelo, Via Cinthia, 80126 Naples, Italy
[4] INAF – Astronomical Observatory of Abruzzo, Via Maggini, 64100 Teramo, Italy
[5] Centre for Astrophysics & Supercomputing, Swinburne University of Technology, Hawthorn, VIC 3122, Australia
[6] European Southern Observatory, Karl–Schwarzschild-Strasse 2, 85748 Garching bei München, Germany
[7] INAF – Osservatorio Astronomico di Padova, Vicolo dell'Osservatorio 5, 35122 Padova, Italy
[8] INAF – Astronomical Observatory of Padova, Via dell'Osservatorio 8, 36012 Asiago, (VI), Italy
[9] Department of Physics, University of Oxford, Denys Wilkinson Building, Keble Road, Oxford OX1 3RH, UK
[10] European Southern Observatory, Alonso de Cordova 3107, Vitacura, Santiago, Chile
[11] Space Physics and Astronomy Research Unit, University of Oulu, PO Box 3000, 90014 Oulu, Finland
[12] Instituto de Astrofísica, Facultad de Física, Pontificia Universidad Católica de Chile, Av. Vicuña Mackenna 4860, 7820436 Macul, Santiago, Chile
[13] INAF – Astronomical Observatory of Rome, Via Frascati, 33, 00078 Monte Porzio Catone, Rome, Italy

Received 4 October 2021 / Accepted 13 June 2022

ABSTRACT

In this work, we extend the catalog of low-surface brightness (LSB) galaxies, including ultra-diffuse galaxy (UDG) candidates, within $\approx 0.4 R_{\rm vir}$ of the Hydra I cluster of galaxies based on deep images from the VST Early-type GAlaxy Survey (VEGAS). The new galaxies were found by applying an automatic detection tool and carrying out additional visual inspections of g and r band images. This led to the detection of 11 UDGs and 8 more LSB galaxies. For all of them, we assessed the cluster membership using the color–magnitude relation derived for early-type giant and dwarf galaxies in Hydra I. The UDGs and new LSB galaxies found in Hydra I span a wide range of central surface brightness ($22.7 \lesssim \mu_{0,g} \lesssim 26.5$ mag arcsec^{-2}), effective radius ($0.6 \lesssim R_{\rm e} \lesssim 4.0$ kpc), and color ($0.4 \leq g-r \leq 0.9$ mag), and have stellar masses in the range $\sim 5 \times 10^6 - 2 \times 10^8\, M_\odot$. The 2D projected distribution of both galaxy types is similar to the spatial distribution of dwarf galaxies, with over-densities in the cluster core and north of the cluster center. They have similar color distribution and comparable stellar masses to the red dwarf galaxies. Based on photometric selection, we identify a total of nine globular cluster (GC) candidates associated to the UDGs and four to the LSB galaxies, with the highest number of candidates in an individual UDG being three. We find that there are no relevant differences between dwarfs, LSB galaxies, and UDGs: the structural parameters (i.e., surface brightness, size, color, and n-index) and GC content of the three classes have similar properties and trends. This finding is consistent with UDGs being the extreme LSB tail of the size–luminosity distribution of dwarfs in this environment.

Key words. galaxies: clusters: individual: Hydra I – galaxies: photometry – galaxies: dwarf – galaxies: formation – galaxies: evolution

1. Introduction

The study of the low-surface brightness (LSB) galaxies in the Universe represents a crucial step in mapping the bottom-up assembly processes of galaxies in all environments, and thus constraining their formation within the lambda-cold dark matter (LCDM) paradigm (Springel et al. 2005). In this framework, the ultra-diffuse galaxies (UDGs) have a special role. They are considered the extreme tail of the size–luminosity distribution of LSB galaxies, being faint ($\mu_{0,g} \geq 24$ mag arcsec^{-2}) and diffuse ($R_{\rm e} \geq 1.5$ kpc) objects, with stellar masses similar to those of dwarf galaxies, $M_* \sim 10^7 - 10^8\, M_\odot$ (van Dokkum et al. 2015). Given the extremely low baryonic mass density, UDGs are particularly suitable laboratories for testing the dark-matter (DM) theories (e.g., Silk 2019; Sales et al. 2020).

However, the detection and analysis of UDGs is challenging because of their LSB nature. Deep imaging surveys brought attention to an ever-increasing detection of UDGs in clusters (Yagi et al. 2016; van der Burg et al. 2017; Zaritsky et al. 2019; Lee et al. 2020; Janssens et al. 2017, 2019; Venhola et al. 2017; Mancera Piña et al. 2018, 2019) and groups (Merritt et al. 2016; Trujillo et al. 2017; Forbes et al. 2019, 2020b; Habas et al. 2020), as well as in less-dense environments (Leisman et al. 2017; Prole et al. 2019b; Román et al. 2019; Habas et al. 2020; Venhola et al. 2022). Based on their observed color distribution, it seems that two populations of UDGs are found: the red and

quenched UDGs, located primarily in clusters of galaxies, but also recently in low-density environments (Marleau et al. 2021), and a blue population of UDGs, which are mostly found in low-density regions (e.g., Leisman et al. 2017; Román & Trujillo 2017a; Marleau et al. 2021).

Because of their LSB nature, there are only a few spectroscopic observations of UDGs, which strongly limits the scope for firm conclusions about the nature of their stellar populations. The few available spectroscopic studies reveal the existence of both metal-poor ($-0.5 \leq [M/H] \leq -1.5$ dex) and old systems (about 9 Gyr; e.g., Ferré-Mateu et al. 2018; Fensch et al. 2019; Pandya et al. 2018; Müller et al. 2020), and younger star-forming UDGs (Martín-Navarro et al. 2019). Based on the few kinematical measurements of UDGs in groups and clusters, only dispersion-dominated systems are known (Emsellem et al. 2019, and references therein).

Particular interest is devoted to the globular cluster (GC) systems in UDGs. Observations suggest that there is clearly a large number of GCs in some UDGs. For massive galaxies, the GCs specific frequency S_N, that is, the number of GCs ($N_{\rm GC}$) per unit of V-band luminosity ($S_N = N_{\rm GC} 10^{0.4[M_v+15]}$, Harris & van den Bergh 1981), is used as a tracer of the host galaxy halo virial mass (e.g., Georgiev et al. 2010; Hudson et al. 2014; Burkert & Forbes 2020). The validity of the GC-versus-halo mass relation in the LSB regime is still to be confirmed (Burkert & Forbes 2020).

Nevertheless, assuming that it also holds for UDGs, in the Coma cluster of galaxies, S_N appears to be larger in UDGs than in dwarf galaxies of similar luminosity (Lim et al. 2020; Forbes et al. 2020a), which could indicate the presence of DM halos more massive for this class of objects than for dwarfs of similar luminosity ($M_h \geq 10^{11}\,M_\odot$). On the other hand, UDGs with S_N similar to that of dwarf galaxies are found in other clusters of galaxies (Prole et al. 2019a; Saifollahi et al. 2021, 2022; Marleau et al. 2021). In this respect, the DM content of the UDGs is one of the most highly debated open issues. Using spectroscopy in addition, a larger DM amount was inferred for a number of UDGs (e.g., Toloba et al. 2018; van Dokkum et al. 2019; Forbes et al. 2020a, 2021; Gannon et al. 2021) while, on the contrary, some others with very low DM content have also been discovered (e.g., van Dokkum et al. 2018; Collins et al. 2021).

The wide range of observed properties for UDGs listed above does not fit in a single formation scenario (see Jones et al. 2021, for a recent summary of various formation processes). There remains a general consensus that different formation channels can result in galaxies with UDG-like properties. To account for the high DM content and large effective radii of the first discovered UDGs, which are comparable to normal Milky Way (MW)-like galaxies, van Dokkum et al. (2015) termed these objects as "failed" galaxies, assuming that this new class of galaxies might have lost gas supply at an early epoch, which prevented the formation of normal, higher surface-brightness systems. The formation of UDGs was also connected to different internal processes such as *(i)* repeated episodes of star formation feedback, which induce kinematical heating of their stars (e.g., Di Cintio et al. 2017), or *(ii)* anomalously high spins of DM halos, which prevent efficient collapse of the gas and therefore the formation of a dense structure (Amorisco & Loeb 2016; Rong et al. 2017; Tremmel et al. 2019). The latter two proposed mechanisms form UDGs with stellar masses and DM fraction comparable with those of dwarf galaxies.

Gravitational interactions and merging between galaxies have also been invoked as possible formation mechanisms for UDGs. Merging of low-mass galaxies at an early epoch could result in a present-day UDG in the field (Wright et al. 2021). UDGs may also have a tidal origin. High-velocity galaxy collisions could induce the formation of DM-free UDGs and, simultaneously, their star clusters (Lee et al. 2021). Diffuse, DM-free, tidal dwarf galaxies (TDGs) are known to form in the tidal tails of strongly interacting galaxies (Lelli et al. 2015; Duc et al. 2014; Ploeckinger et al. 2018). The tidal interaction of a dwarf satellite galaxy in the potential well of a major galaxy might puff it up and lead to the formation of a UDG-like system (Conselice 2018; Carleton et al. 2019, 2021). Recently, based on deep optical images of the Fornax cluster, Venhola et al. (2022) found that the spatial distributions of UDGs and LSB dwarfs are more concentrated in the cluster core than that of the normal dwarfs, and that UDGs and LSB dwarfs show more morphological signs of tidal interactions than other galaxies. There are few cases of UDGs potentially associated with faint stellar streams detected in the outskirts of galaxies in a group environment, suggesting that UDGs might also form from material released during a weak tidal interaction (Bennet et al. 2018; Müller et al. 2019; Montes et al. 2020). Finally, Poggianti et al. (2019) suggested that the DM-free UDGs might form from ram pressure stripped (RPS) gas clumps in the extended tails of infalling cluster galaxies, depending on their subsequent dynamical evolution. A UDG candidate that might have formed from the RPS gas clumps was recently discovered by Iodice et al. (2021) in NGC 3314A, a Hydra I cluster member. Confirmation of the nature of this UDG through follow-up spectroscopy could be the missing observational evidence of this formation channel.

High-resolution hydrodynamical cosmological simulations were recently developed to resolve the internal structure of low-mass galaxies in clusters, and were used to trace the formation and evolution of LSB galaxies. Based on the IllustrisTNG simulations, Sales et al. (2020) also proposed two different formation channels for UDGs. A population of "genuine" LSB galaxies with UDG properties could form in the field and later enter the cluster environment. The so-called tidal-UDGs (T-UDGs) stem from luminous galaxies and evolve into UDGs due to cluster tidal forces that remove their DM fraction and puff up their stellar component. The T-UDGs populate the center of the clusters and, at a given stellar mass, have lower velocity dispersion, higher metallicity and lower DM fraction with respect to the genuine UDGs. Using the RomulusC simulations, Tremmel et al. (2020) suggested that UDGs could form from dwarf galaxies, where the gas was removed and the star formation was halted by the ram pressure acting during their motions through the cluster. Recently, Benavides et al. (2021) proved that quenched and isolated UDGs are formed as backsplash galaxies, which were satellites of a group or a cluster halo in an early epoch, and were today found a few megaparsecs away from them. This kind of interaction would remove the gas and tidally strip the outskirts of the DM halo.

In summary, both the observational and theoretical works on UDGs cited above show that more than one formation channel might exist for this class of objects, leading to different structural properties (e.g., colors, stellar populations, and DM fraction), perhaps also depending on the environment where they reside. Therefore, to shed light on this aspect, deep imaging and spectroscopy must be collected for complete samples of UDGs across different environments in order to systematically explore their properties from the densest regions in the cores of clusters, out to their less populated outskirts, and in the field. Because of their LSB nature, which could prevent their systematic detection, a complete sample of UDGs is meant to be the expected number

density of UDGs in the host environment, based on the relation published by van der Burg et al. (2017) and Janssens et al. (2019), times the environment virial mass. With the present paper, we provide a complete sample of UDGs in the Hydra I cluster and analyze their structural photometric properties. This work builds on the previous studies of the Hydra I cluster by La Marca et al. (2022, hereafter Paper I) who presented a new catalog of 317 dwarf galaxies fainter that $M_r \geq -18.5$ mag, and by Iodice et al. (2020). The latter provided the first sample of 20 LSB galaxies, with $\mu_{0,g} \geq 23.5$ mag arcsec^{-2} and $R_e \geq 0.6$ kpc, of which 12 have been classified as UDGs in this cluster. Nevertheless, in this work we consider true UDGs to be those galaxies that rigorously respect the van Dokkum UDG definition. Therefore, here, we only count 9 of the 20 LSB galaxies presented by Iodice et al. (2020) as genuine UDGs. In addition, one more UDG in the Hydra I cluster has been discovered in the stellar filaments of NGC3314A (hereafter referred to as UDG32, Iodice et al. 2021), bringing the total number of currently known UDGs in this cluster to 10.

The Hydra I cluster has a virial mass of $M_{200} = 2.1 \times 10^{14}\, h^{-1}\, M_\odot$, as estimated from X-ray observations of the intracluster medium (Tamura et al. 2000). It is located in the southern hemisphere at a distance of 51 ± 6 Mpc (Christlein & Zabludoff 2003). Recent studies show that the core of the cluster reveals ongoing interactions that trace the extended mass assembly around the brightest cluster member NGC 3311 (see Barbosa et al. 2018, and references therein). As found in Paper I, most of the dwarf galaxies in the cluster are concentrated in the core and around a subgroup of galaxies in the north. These are the two densest regions of the cluster, which show signs of galaxy interactions and presence of intra-cluster diffuse light (Iodice et al. in prep.). Therefore, the Hydra I cluster offers an exquisite opportunity to analyze this class of LSB galaxies as a function of the environment and relate them to the mass-assembly processes.

The paper is organized as follows. The Hydra I imaging data used in this paper are introduced in Sect. 2, while the detection of new UDG candidates is presented in Sect. 3. In Sect. 4 we explain how we detected and selected possible GCs for our sample of UDGs, and in Sect. 5 we report the results of our analysis: the spatial distribution of UDGs, their photometric properties, and their GC candidates. Finally, in Sect. 6 we discuss the properties of the UDGs in the Hydra I cluster, while conclusions are provided in Sect. 7.

2. Data: deep images of the Hydra I cluster

The imaging data for the Hydra I cluster presented in this work were collected in the g and r bands with the European Southern Observatory (ESO) VLT Survey Telescope (VST) as part of the VST Early-type Galaxy Survey (VEGAS[1]). The optical camera OmegaCAM (Kuijken 2011) on the VST records wide-field images spanning a 1×1 deg^2 field of view, with a pixel scale of 0.21 arcsec/pixel. The observing strategy and data reduction were presented by Iodice et al. (2020) and in Paper I. Briefly, images were acquired in dark time, with total integration times of 2.8 and 3.22 hours in the g and r bands, respectively. The VST mosaic covers an area of $1^\circ \times 2^\circ$ (0.9×1.8 Mpc at the distance of the cluster) around the cluster core. As described by Iodice et al. (2020) and in Paper I, the observing strategy and data reduction, coupled with the long integration times and the large covered area allow us to study the Hydra I cluster down to the LSB regime out to $\approx 0.4 R_{vir}$. In particular, during the data acquisition, in order to reduce the scattered light from the bright (seventh-magnitude) foreground star, which is on the NE side of the cluster core, this star was always put in one of the two wide OmegaCam gaps. The residual light from this bright star has been modeled and subtracted from the reduced mosaic, in both bands. Also, the light distribution of the second brightest star in the field, located SE of the core, is accounted for by modeling and subtracting it from the parent image (see Fig. 1 in Iodice et al. 2020). We estimate surface brightness depths of $\mu_g = 28.6 \pm 0.2$ mag arcsec^{-2}, and $\mu_r = 28.1 \pm 0.2$ mag arcsec^{-2} for the final stacked images. These depths are derived as the flux corresponding to 5σ, with σ averaged over 1 arcsec^2 of empty area.

The automatic detection of LSB galaxies in Hydra I has been improved and is described in Paper I, where we compiled a new catalog counting 317 dwarf galaxies fainter than $M_r \geq -18.5$ mag[2]. A dwarf galaxy catalog on a smaller area was presented by Misgeld et al. (2008), containing galaxies with $M_V \geq -17$ mag. In the present paper, we focus on the new LSB galaxies detected in the cluster, including UDG candidates. All magnitudes and colors are corrected for Galactic extinction using values from Schlafly & Finkbeiner (2011).

3. Discovery of new LSB galaxies and UDG candidates

As detailed in Paper I, we run the automatic tool SExtractor (Bertin & Arnouts 1996) on the VST mosaic to detect the LSB galaxies in the Hydra I cluster. We tuned SExtractor parameters by setting the *THRESHOLD* to five times the background noise standard deviation, the minimum area[3] to 25 pixels, and the background model grid size to 256×256 pixels. In this work, to improve the detection of LSB galaxies, we adopted the following steps: *(i)* the light distribution of the brightest cluster members was modeled and subtracted from the parent image (Iodice et al., in prep.); *ii)* on the residual image we made another SExtractor run, setting the *THRESHOLD* parameter to one time the background noise standard deviation; *(iii)* a complementary visual inspection was then performed on the images, revealing new LSB galaxies, which were not detected by SExtractor; and *(iv)* the cluster membership of detected galaxies is inferred using the color–magnitude relation (CMR) for early-type giant and dwarf galaxies in Hydra I (Misgeld et al. 2008). This CMR is converted from the Johnson V and I bands to the SDSS g and r photometric bands using the conversion factors given by Kostov & Bonev (2018). The band-conversion equations are:

$$V = r - 0.017 + 0.492 \cdot (g-r), \quad (1)$$

$$V - I = 0.27 + 1.26 \cdot (g-r). \quad (2)$$

Only the LSB galaxies consistent with the assumed CMR, within the errors, are kept in our final sample. Galaxies with colors redder than 2σ from the CMR derived by Misgeld et al. (2008)

[1] See http://www.na.astro.it/vegas/VEGAS/Welcome.html

[2] As detailed in Paper I, at $M_B \simeq -18$ mag a separation between dwarfs and giants ellipticals emerges in the $\langle\mu\rangle - L$ plane. The early-type dwarfs fainter than $M_B \simeq -18$ mag in general do not share the surface brightness–luminosity relation defined by giant ellipticals (Binggeli & Cameron 1991). Hence, considering the typical $B-r$ colors for early-type dwarfs ≥0.5 mag, we assumed $M_r = -18.5$ mag as the limit for dwarf galaxies.

[3] The minimum area parameter corresponds to the number of connected pixels above the threshold to have a detection.

Table 1. Parameters of the new UDG candidates in the Hydra I cluster.

Object	RA	Dec	Detection	$M_{r,0}$	$(g-r)_0$	M/L_r	M_*	μ_e	μ_0	R_e	n	$\tilde{\chi}^2$
	[deg]	[deg]		[mag]	[mag]		[$10^7\,M_\odot$]	[mag arcsec^{-2}]	[mag arcsec^{-2}]	[kpc]		
(1)	(2)	(3)	(4)	(5)	(6)	(7)	(8)	(9)	(10)	(11)	(12)	(13)
UDG 13	159.060384	−27.507390	V	−12.73	0.64 ± 0.30	2.00 ± 1.00	2.0 ± 1.0	27.35 ± 0.11	24.23 ± 0.20	1.60 ± 0.20	1.70 ± 0.06	6.3
UDG 14	159.000949	−27.544729	A	−11.91	0.70 ± 0.30	2.00 ± 2.00	1.1 ± 0.8	28.50 ± 0.04	24.50 ± 0.50	1.83 ± 0.12	2.0 ± 0.2	1.1
UDG 15	159.010624	−27.605435	V	−11.95	0.50 ± 0.30	1.20 ± 0.80	0.6 ± 0.4	27.70 ± 0.20	25.01 ± 0.30	1.51 ± 0.15	1.40 ± 0.10	11.0
UDG 16	159.10242	−27.235641	V	−12.84	0.43 ± 0.20	1.00 ± 0.50	1.1 ± 0.5	27.63 ± 0.11	25.90 ± 0.20	1.75 ± 0.12	0.97 ± 0.09	1.0
UDG 17	159.173845	−27.277078	V	−13.99	0.86 ± 0.11	4.00 ± 1.00	12 ± 3.0	26.70 ± 0.08	24.90 ± 0.10	1.50 ± 0.20	1.00 ± 0.10	1.6
UDG 18	159.070065	−27.338011	V	−12.28	0.52 ± 0.20	1.30 ± 0.60	0.9 ± 0.4	27.60 ± 0.20	25.56 ± 0.19	1.64 ± 0.12	1.08 ± 0.03	1.7
UDG 19	159.010682	−27.290000	V	−11.49	0.80 ± 0.20	3.00 ± 1.00	1.0 ± 0.5	28.50 ± 0.20	26.50 ± 0.30	1.98 ± 0.12	1.10 ± 0.13	1.1
UDG 20	159.518455	−27.497272	A	−12.95	0.49 ± 0.05	1.20 ± 0.14	1.4 ± 0.2	27.33 ± 0.15	26.03 ± 0.33	1.97 ± 0.12	0.79 ± 0.12	1.4
UDG 21	159.225691	−27.615297	A	−12.78	0.45 ± 0.10	1.00 ± 0.20	1.1 ± 0.3	27.30 ± 0.50	24.00 ± 0.40	1.50 ± 0.12	1.70 ± 0.15	1.5
UDG 22	158.670717	−27.700909	A	−13.92	0.50 ± 0.05	1.23 ± 0.14	3.6 ± 0.4	26.50 ± 0.14	25.26 ± 0.18	3.60 ± 0.12	0.72 ± 0.08	1.0
UDG 23	158.865410	−27.771273	A	−14.11	0.42 ± 0.02	0.96 ± 0.04	3.4 ± 0.2	27.20 ± 0.20	24.29 ± 0.30	2.47 ± 0.20	1.5 ± 0.14	6.0

Notes. Column 1 reports the name of the UDG candidate. In Cols. 2 and 3 we list the coordinates of the UDGs in J2000. In Col. 4 we report the kind of detection, i.e. visual inspection (flag "V") or by the automatic tool (flag "A"). In Cols. 5 and 6 we report the total r-band magnitude and the average $g-r$ color. Columns 7 and 8 give the stellar mass-to-light ratio derived in the r band and stellar mass, respectively. Columns 9–12 list the structural parameters derived from the 2D fit in the g band: the effective and central surface brightness, the effective radius in kpc and the n exponent of the Sérsic law, respectively. In Col. 13 we report the value of $\tilde{\chi}^2$, which indicates the goodness of the fit of the surface brightness profiles. Magnitudes and colors are corrected for Galactic extinction using values from Schlafly & Finkbeiner (2011).

Table 2. Parameters of the new LSB galaxies in the Hydra I cluster.

Object	RA	Dec	Detection	$M_{r,0}$	$(g-r)_0$	M/L_r	M_*	μ_e	μ_0	R_e	n	$\tilde{\chi}^2$
	[deg]	[deg]		[mag]	[mag]		[$10^7\,M_\odot$]	[mag arcsec^{-2}]	[mag arcsec^{-2}]	[kpc]		
(1)	(2)	(3)	(4)	(5)	(6)	(7)	(8)	(9)	(10)	(11)	(12)	(13)
LSB 1	159.000120	−27.482826	V	−12.38	0.40 ± 0.30	0.90 ± 0.60	0.60 ± 0.40	26.59 ± 0.13	23.90 ± 0.20	0.81 ± 0.90	1.38 ± 0.08	16.0
LSB 2	159.040202	−27.514335	V	−12.87	0.53 ± 0.20	1.30 ± 0.60	1.50 ± 0.70	25.84 ± 0.07	23.80 ± 0.14	0.57 ± 0.12	1.10 ± 0.07	1.4
LSB 3	159.110634	−27.544892	V	−12.03	0.41 ± 0.30	0.90 ± 0.60	0.50 ± 0.30	26.60 ± 0.80	23.69 ± 0.60	0.70 ± 0.12	1.50 ± 0.20	2.0
LSB 4	159.084460	−27.231646	A	−13.83	0.41 ± 0.30	0.90 ± 0.60	2.50 ± 1.80	26.55 ± 0.06	24.73 ± 0.09	1.48 ± 0.12	1.00 ± 0.03	2.0
LSB 5	159.171918	−27.805707	A	−13.74	0.58 ± 0.02	1.59 ± 0.07	4.00 ± 0.20	25.81 ± 0.01	23.93 ± 0.03	1.42 ± 0.12	1.03 ± 0.01	1.6
LSB 6	159.519470	−27.545830	A	−15.47	0.56 ± 0.02	1.49 ± 0.07	18.40 ± 0.90	26.02 ± 0.08	23.00 ± 0.20	4.00 ± 1.00	1.56 ± 0.11	1.1
LSB 7	159.077907	−27.621647	A	−15.68	0.62 ± 0.02	1.80 ± 0.08	25.89 ± 0.02	25.30 ± 0.01	22.70 ± 0.02	1.97 ± 0.10	1.36 ± 0.01	1.5
LSB 8	159.476947	−27.258645	A	−15.27	0.54 ± 0.02	1.40 ± 0.06	14.40 ± 0.70	25.12 ± 0.11	23.20 ± 0.20	1.51 ± 0.20	1.05 ± 0.08	1.5

Notes. Same as Table 1, but for the new LSB galaxies of the sample.

are excluded. We consider it highly unlikely that the LSB galaxies are members of other foreground or background structures and are only projected along the line of sight towards Hydra I by chance. Indeed, as also discussed in Paper I, there is evidence of a 40–50 Mpc under-dense region in front of and behind the Hydra I cluster, along the line of sight (Richter et al. 1982; Richter 1987).

As a result of our new search, 19 new LSB galaxies have been added to the catalog of LSB candidates recently presented in Paper I. These are listed in Tables 1 and 2. Their projected location in the cluster is shown in Fig. 1. For all the new candidates, we performed the surface photometry to derive the structural parameters as described below.

In the cutout extracted from the VST mosaic around each new LSB galaxy, we identified all the background and foreground objects (stars and galaxies) brighter than the 2σ background level. The most extended ones (i.e. ≥ 2 times the LSB in the cutout) are modeled by adopting an isophote fit (where all parameters are left free to vary) and are then subtracted from the image. All the remaining objects are carefully masked. Once all bright objects are masked or modeled and subtracted, we performed the isophote fit for each LSB galaxy of the sample using the ASTROPY package PHOTUTILS (Bradley et al. 2020) in the g and r bands. The ellipticity of the isophotes is also fitted rather than using a fixed value. From the azimuthally averaged surface brightness profiles, a local background value is estimated for each object (see Iodice et al. 2021, for details). Briefly, the local background is computed in an outer annulus where the light blends into the average scatter of the residual sky level.

For all candidates in the new sample, the structural parameters (i.e., central surface brightness μ_0 and effective radius R_e) are derived by fitting the g-band azimuthally averaged profile, which sums up the light at the faintest levels with a single Sérsic function (Sérsic 1963). The best fit is obtained by adopting the χ^2 minimization method[4], where a weighted fit is performed, taking into account the error on each data point of the surface brightness profile. Therefore, the data points corresponding to the central regions of the galaxies, with their small uncertainties have considerable weight in determining the best-fit solution. As we are interested in classifying UDGs, this approach can reasonably exclude spurious large values of effective radii, which might bias the selection process. The error estimate on the structural parameters, R_e and μ_0, includes the uncertainties on the fitting, which are about 0.2% and 6%, respectively, and on the sky removal for μ_0 (∼1%, see Iodice et al. 2020), and on the distance (∼12%) for R_e. The structural parameters derived by the best fit and the reduced $\tilde{\chi}^2$, which indicates the goodness of the fit are listed in Tables 1 and 2.

[4] The χ^2 is defined as $\sum_{0\leq i\leq N} \sqrt{[f(x)-D]^2/N}$, where $f(x)$ is the Sérsic law used to fit the observed values (D), and N is the number of the data points. The goodness of the fit is provided by the reduced $\tilde{\chi}^2$, given by $\chi^2/(N - N_{\rm param}) \sim 1$, where $N_{\rm param}$ is the number of fitted parameters (i.e. μ_0, R_e, n).

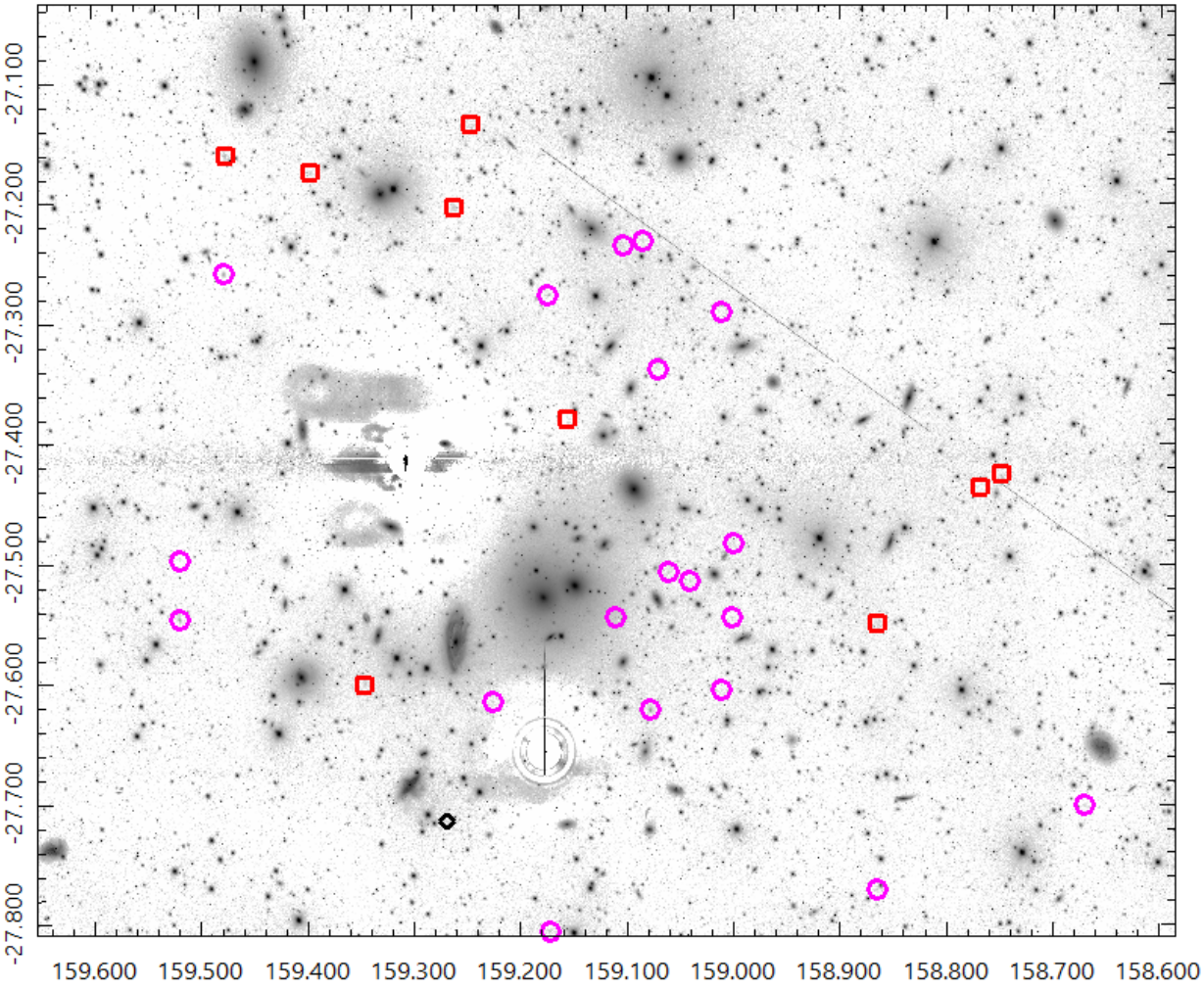

Fig. 1. VST mosaic (56.7′ × 46.55′ ∼0.8 × 0.7 Mpc) of the Hydra I cluster in the g band, corresponding to $\approx 0.4 R_{\rm vir}$. The 19 new galaxies detected in this work are marked as magenta circles. Red boxes show the first sample of UDGs presented by Iodice et al. (2020) and the black diamond marks the position of UDG32 reported by Iodice et al. (2021). North is up and east to the left.

We derived the growth curve from the isophote fit for all the newly detected LSB galaxies in the Hydra I cluster. These are shown in Appendices C and D. From the growth curve, we computed the total integrated magnitudes in the g and r bands, and the effective radius $R_{\rm e}^{50}$, as the distance from the galaxy center containing half of the light. For all galaxies of the sample, the values of $R_{\rm e}^{50}$ (see Figs. C.5 and C.6, and Figs. D.4 and D.5) are consistent with the values of $R_{\rm e}$ estimated by the best fit of the surface brightness profiles. This is particularly important for those galaxies where the fit appears quite poor ($\tilde{\chi}^2 \geq 2$), as described in Sect. 3.1, as this provides a robust estimate of the $R_{\rm e}$, which is independent from any fitting law.

The $g-r$ color obtained by the integrated magnitudes and the absolute magnitude in the r band (M_r) are then used to derive the stellar mass for all LSB galaxies, using the relation given by Into & Portinari (2013), where $\log(M/L_r) = 1.373 \times (g-r) - 0.596$.

Nine of the new galaxies were found only by visual inspection. These are the smallest (semi-major axis radius $R \leq 8$ arcsec ∼2 kpc) and/or most diffuse objects of the sample, with effective g-band surface brightness $\mu_{\rm e}$ ranging from ∼26 to 28.5 mag arcsec^{-2} (see Tables 1 and 2). Most of the visually detected galaxies do not show a steep increase of the surface brightness toward the galaxy center, as observed for all those found by SExtractor, which have $25 \lesssim \mu_{\rm e} \lesssim 28.5$ mag arcsec^{-2}, and are also the most extended objects of the sample ($R_{\rm e}$ up to 16 arcsec ≃4 kpc).

3.1. New UDGs in the Hydra I cluster

As stated in Sect. 1, van Dokkum et al. (2015) empirically defined the UDGs to be faint, with $\mu_{0,g} \geq 24$ mag arcsec^{-2} and diffuse, with $R_{\rm e} \geq 1.5$ kpc. Other criteria have been proposed in literature, which used different cuts in size and/or surface brightness limits (Koda et al. 2015; Mihos et al. 2005; Yagi et al. 2016; van der Burg et al. 2017). Recently, Lim et al. (2020) adopted a new selection method to classify UDGs in the Virgo cluster based on the scaling relations between photometric and structural properties of LSB galaxies (e.g., total luminosity vs. $R_{\rm e}$ and $\mu_{\rm e}$). According to this selection method, UDGs are identified as "outliers" in the scaling relationships, being 2.5σ fainter and larger than the average distribution of the parent LSB sample.

In this work, in order to be consistent with the previous UDGs study in the Hydra I cluster (Iodice et al. 2020, 2021), and to compare the UDG properties with those published by

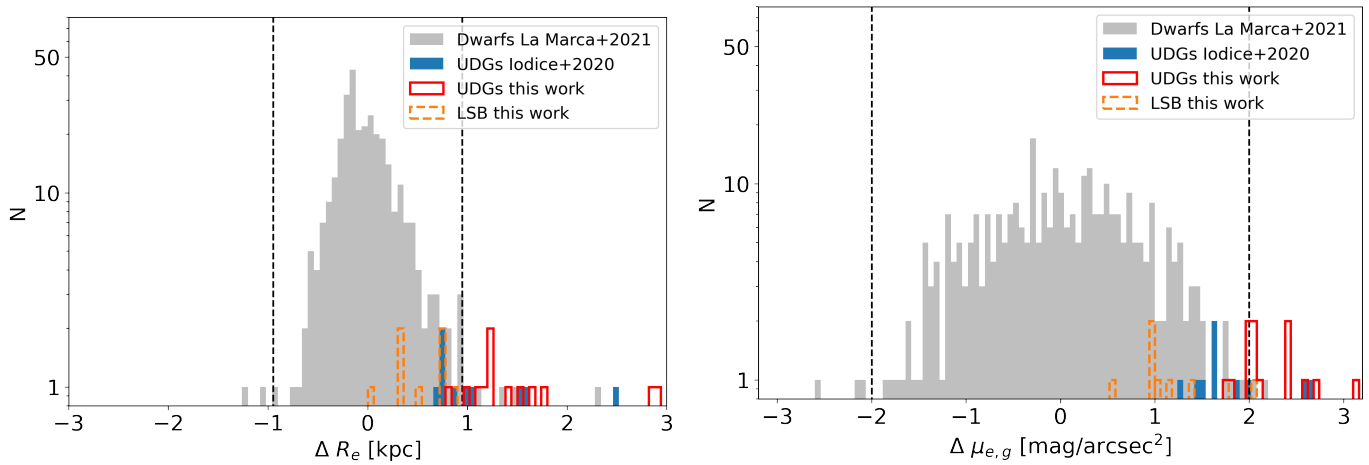

Fig. 2. Deviations from the mean relation between luminosity and effective radius (*left panel*), and from the mean relation between luminosity and effective surface brightness (*right panel*). Vertical dashed lines show the 2.5σ deviations from the mean relations.

several other papers (see Sect. 7), we decided to adopt the empirical definition proposed by van Dokkum et al. (2015), that is, $R_e \geq 1.5$ kpc and $\mu_0 \geq 24$ mag arcsec^{-2} in g band, derived by the fit of the light distribution using a Sérsic law. Hence, from the whole sample of 19 new LSB galaxies, the selection process led to 11 UDGs in the Hydra I cluster (see Fig. 1). These are listed in Table 1, which includes the structural parameters and the detection method (i.e., SExtractor or visual inspection).

Using the selection method proposed by Lim et al. (2020) we found a comparable number of UDGs. In Fig. 2 we show the distribution of the deviations from the mean relations between luminosity and effective radius and surface brightness of dwarf galaxies (ΔR_e and $\Delta\mu_e$) for the whole sample of dwarf and LSB galaxies in the Hydra I cluster (from Paper I, Iodice et al. 2020, 2021, and this work). Of these, 25 galaxies are found to deviate by more than 2.5σ for at least one of the two mean scaling relations. Of these 25 galaxies, 17 are 2.5σ fainter and larger than both the average fitted distributions. Therefore, according to Lim et al. (2020), 17 galaxies would be defined as *primary* UDGs, and 8 as *secondary* UDGs. Of the 17 *primary* UDGs, 13 also respect the van Dokkum et al. (2015) empirical definition.

In the sample of 11 new UDGs in Hydra I, three (UDG 13, UDG 15 and UDG 23) are poorly fitted with a single Sérsic function, and a second component would be required. This is not done here, because we aim to consistently compare the structural properties of all UDGs in Hydra I with those of UDGs in other clusters of galaxies, which are obtained by adopting a single Sérsic function. Nevertheless, for the three UDGs listed above, the R_e^{50} derived by the growth curve is larger than 1.5 kpc, and is consistent with the R_e estimated by the best fit. Therefore, they can be safely identified as UDGs. It is worth noting that these UDGs might host a diffuse and faint halo in the galaxy outskirts. Something similar was recently observed by Gannon et al. (2021) for a UDG in a loose group of galaxies.

The sample of new UDGs is displayed on the CMR in Fig. 3. In Fig. 4 we show the photometric parameters for the new UDG candidates as a function of their effective radius. In both plots, the new UDGs are compared with those from the previous sample of ten UDGs detected in Hydra I, and with the sample of Hydra I dwarf galaxies (Paper I and Misgeld et al. 2008). In Appendix C we show the individual UDG images and the azimuthally averaged surface brightness profile in the g band, including the best-fit model.

The green triangle in the UDG area of the $\mu_0 - R_e$ plane is HCC 087, which was originally classified as an early-type dwarf in the Hydra Cluster catalog by Misgeld et al. (2008). Its large R_e and low surface brightness are the result of strong tidal features detected around a dwarf spheroidal galaxy with ongoing tidal disruption (Koch et al. 2012). We decided not to include this target in the final UDG sample because of its conspicuous S-shape and clear signs of tidal disruption, which is quite different from other UDG candidates that have more rounded shapes (see Appendix C).

The new UDGs have $(g-r)_0$ color in the range 0.4−0.86 mag, with an average value of $(g-r)_0 = 0.57 \pm 0.15$ mag. The stellar mass ranges from $\sim 6 \times 10^6$ to $\sim 1.2 \times 10^8$ $M_\odot$ (see Table 1).

3.2. New LSB galaxies in the Hydra I cluster

The structural parameters of the remaining eight newly detected LSB galaxies are listed in Table 2. They show a wide range of values in effective radius, $0.6 \lesssim R_e \lesssim 4.0$ kpc, and surface brightness, $22.7 \lesssim \mu_{0,g} \lesssim 24.73$ mag arcsec^{-2}. Six of them have larger size ($R_e \geq 1.2$ kpc) and fainter central surface brightness than typical dwarf galaxies of similar luminosity, and therefore resemble large LSB dwarfs. Three of them are located in the transition region between the dwarf galaxies and the UDG (i.e., $\mu_0 \simeq 24$ mag arcsec^{-2} and $R_e \simeq 1.5$ kpc, see Fig. 4). Taking into account the 1σ error on the structural parameters, which are ∼0.03−0.6 mag arcsec^{-2} for μ_0 and ∼0.12 kpc for R_e, these galaxies might fall in the UDGs region of the R_e vs. μ_0 plane. This means that a definitive conclusion on the nature of these galaxies cannot be provided based on photometry alone. Spectroscopic data are necessary to reduce the uncertainties on R_e – once redshift is estimated – and to constrain the stellar population content.

The g-band images, including surface brightness profiles and their best fit, are provided in Appendix D. The surface brightness profiles of two objects (LSB 6 and LSB 7) show a bright central component (with $R_e \sim 0.5-1.7$ kpc, see Figs. D.2 and D.3) resembling a small bulge, in addition to a shallower and extended component at larger radii. Therefore, for these objects, the best fit of the light distribution would be obtained with the superposition of two Sérsic profiles. However, to be consistent with the selection method adopted in this paper, we used the structural parameters derived by fitting a single Sérsic law.

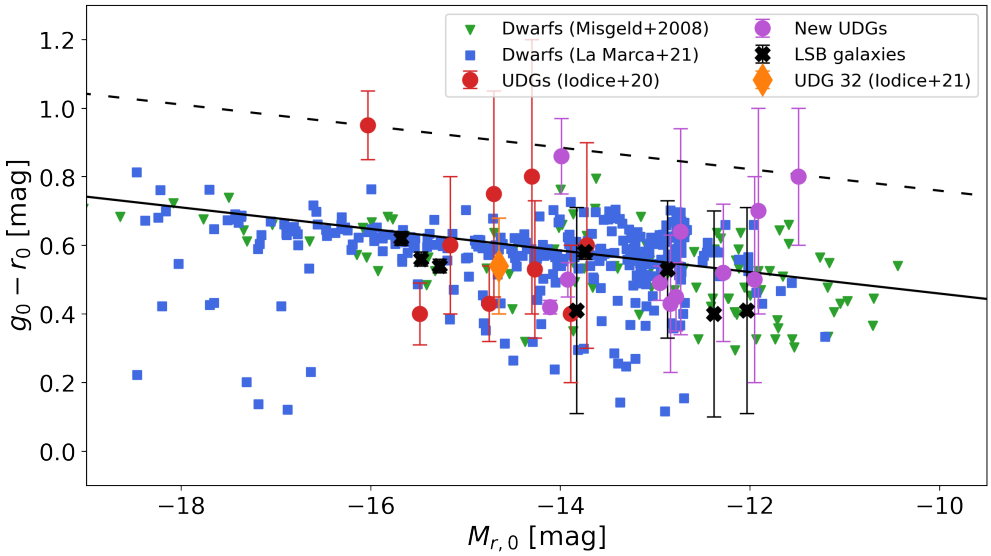

Fig. 3. Color–magnitude diagram for the full sample of dwarfs, LSB galaxies, and UDGs detected in the VST Hydra I mosaic. The newly detected UDGs are shown as magenta filled circles, while black crosses indicate the new LSB galaxies. Blue filled squares are dwarf galaxies presented in Paper I, red points are the UDGs found by Iodice et al. (2020), and the green triangles are the Hydra I galaxies presented by Misgeld et al. (2008). The solid black line is the CMR for the Hydra I cluster early-type galaxies, with its upper 2σ scatter limit (dashed line), as derived by Misgeld et al. (2008): $(g{-}r) = -0.0314 \cdot M_r + 0.145$, $\sigma = 0.15$.

Compared to the UDGs, these LSB galaxies have similar range of $(g{-}r)_0$ color, with $0.41 \leq (g{-}r)_0 \leq 0.62$ mag, and a fully consistent average value of $(g{-}r)_0 = 0.51 \pm 0.08$ mag. The stellar masses are also mostly similar with those derived for UDGs, in the range $\sim 5 \times 10^6$ to $\sim 4 \times 10^7\, M_\odot$, except for three objects, which are one order of magnitude more massive ($\gtrsim 10^8\, M_\odot$, see Table 2).

4. Detection of globular clusters

With our data, that is, deep g- and r-band imaging, two optical and relatively close passbands, it is hard to clearly identify the GC populations because of the expected large foreground and background contamination. Nevertheless, as detailed in the previous VEGAS papers, the large format of the OmegaCam allows us to robustly constrain the background contamination from the analysis of regions at large angular distances from the target(s).

To detect GCs around all the newly detected cluster members – both UDGs and LSB galaxies –, we adopted the same procedure as that described by Iodice et al. (2020), and more extensively presented in Cantiello et al. (2018a, 2020). Briefly, we ran SExtractor on g and r cutouts of $\sim 20R_e \times 20R_e$ in size centered on each galaxy. To improve source detection down to the faintest magnitude levels, we subtracted the galaxy model derived from `GALFIT`. The GCs at the distance of Hydra I in images with a $FWHM \sim 0.8$ arcsec seeing can be considered point sources. For each source and in each band, we derived the following quantities:

- The automated aperture magnitude (MAG_AUTO) to estimate the total magnitude of the source;
- The aperture magnitude (MAG_APER) within 4, 6, and 8 pixels diameter;
- The $g{-}r$ color[5] as:

  $MAG\_APER_g[6_{\rm pix}]{-}MAG\_APER_r[6_{\rm pix}]$;

- and the concentration index as:

  $CI_X = MAG\_APER_X[4_{\rm pix}]{-}MAG\_APER_X[8_{\rm pix}]$,

which is an indicator of source compactness in the X band (Peng et al. 2011).

At the adopted distance of Hydra I, the peak of the GC luminosity function (GCLF), the so-called turn-over magnitude (TOM), is $\mu_{g,\rm TOM} \simeq 26.0$ mag (we assumed $M_g^{\rm TOM} = -7.5$, from Villegas et al. 2010). Adopting a median $\langle g{-}r \rangle = 0.6$ mag for the GC population (Cantiello et al. 2018b), the r-band TOM is $\mu_{r,\rm TOM} \simeq 25.4$ mag. To identify GC candidates, we select sources with: *(i)* g-band magnitude $23.5 \leq m_g \leq 26.0$ mag, the expected range between the TOM of the GCLF and $3\sigma_{\rm GCLF}$ mag brighter ($3\sigma_{\rm GCLF} = 2.5$ mag, Villegas et al. 2010); *(ii)* color $0.25 \leq g{-}r \leq 1.25$ mag[6]; *(iii)* SExtractor star–galaxy classifier: $CLASS\_STAR \geq 0.4$, where we assumed a low CLASS_STAR value for star–galaxy separation, as the classifier becomes less reliable toward the faint magnitudes we are interested in; *(iv)* elongation (i.e., major-to-minor axis ratio from SExtractor) ≤ 2 in both bands; and *(v)* CI_X within ± 0.1 mag of the local sequence of point sources. The choices of 4 and 8 pixels, and $\Delta CI_x = \pm 0.1$ mag, were made after several tests as a compromise between the completeness and contamination (see also Saifollahi et al. 2021, 2022, where the same compactness parameter is adopted).

With these criteria, we identified the GC candidates around each galaxy in the sample, and estimated their local density $\Sigma_{\rm GC}^{\rm UDG}$. To correct for background contamination, we need to characterize the expected number of foreground MW stars, background galaxies, and possible intra-cluster GCs (ICGCs). The

[5] The g and r aperture magnitudes are not aperture corrected. The aperture corrections in the two passbands are nearly identical (~0.35 mag), and so they compensate each other when deriving the $g{-}r$ color, while the total error we estimated on the combined apertures is of the order of ~0.04 mag. In other words, we do not apply any correction as the correction is smaller than its uncertainty.

[6] Based on model predictions from `http://cosmic.yonsei.ac.kr/YEPS.htm`, for ages older than 8 Gyr, Chung et al. (2020), and empirical results from Cantiello et al. (2018b). Similar color limits were adopted by Carlsten et al. (2022).

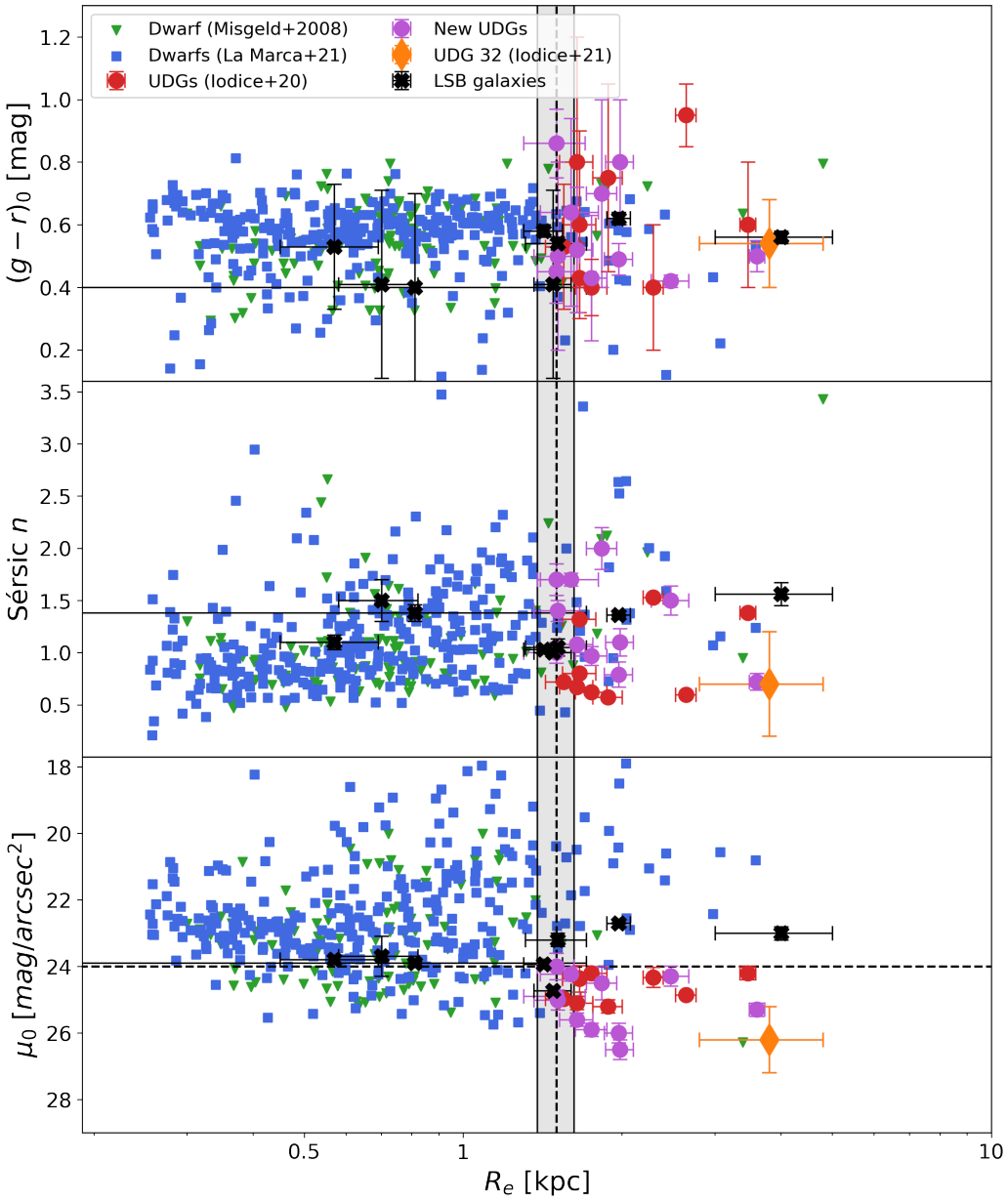

Fig. 4. Structural and photometric parameters for the newly discovered UDGs (filled magenta circles) as a function of the effective radius. Symbols are the same as Fig. 3. The UDG definition criteria, $R_e \geq 1.5$ kpc and $\mu_0 \geq 24$ mag arcsec^{-2} (van Dokkum et al. 2015), are shown by the dashed lines. The vertical shaded region indicates the range of uncertainty on R_e given by the uncertainties on the cluster distance.

stars and background galaxy contamination is most effectively derived in regions far from the virial radius of the cluster. The local effect of ICGCs is instead better constrained around the UDG or LSB galaxy itself. Hence, we obtained two independent characterisations of the background. A local background is derived by running the GC selection criteria on the catalogs of sources detected in annuli of $5R_e \leq r \leq 10R_e$ around each galaxy[7]. We find that the number of GC candidates in such areas is on average $\Sigma_{GC}^{bkgr} = 5.0 \pm 1.5$ per square arcmin, ranging from a minimum of 1.3 arcmin^{-2} to a maximum of 11.5 arcmin^{-2}.

Furthermore, we estimated a global background from five different fields with sizes of $\sim 10' \times 10'$, outside the Hydra I virial radius, free from bright foreground MW stars, and obvious Hydra I cluster galaxies, obtaining a background density of $\Sigma_{GC}^{bkgr} = 1.35 \pm 0.17$ arcmin^{-2}.

We keep both background estimates as the global background is statistically more robust, but it possibly fails to accurately sample the ICGC contamination in UDGs closer to the cluster core; the local background, on the other hand, can better constrain the local ICGC population but it suffers from larger statistical uncertainty.

The physical extent of the GC system around UDGs and LSB galaxies is still subject to debate (Forbes 2017; Müller et al. 2021; Caso et al. 2019; Kartha et al. 2014). Hence, we derived the total number of GCs (N_{GC}) within $1.5R_e$, as in van Dokkum et al. (2016), and also within 3 and $5R_e$. As the

[7] The radius $5R_e$ is considered an upper limit for bound systems (Kartha et al. 2014; Forbes 2017; Caso et al. 2019). The upper limit to $10R_e$ is motivated by the need to have an area enclosing ~20 GC candidates, and sufficiently large to constrain the local background.

photometry roughly reaches the TOM peak (the median photometric uncertainty is $\Delta m_g \simeq 0.2$ mag at $m_g = 26$ mag for point sources) and assuming the LSB galaxy GCLF is a Gaussian (e.g., Rejkuba 2012; van Dokkum et al. 2016), we derived $N_{\rm GC}$ as twice the background-corrected GC density over the 3 and $5R_{\rm e}$ area of the galaxy multiplied by the area: $N_{\rm GC} = 2\times(\Sigma_{\rm GC}^{\rm LSB} - \Sigma_{\rm GC}^{bkgr})\times Area$[8]. When estimating the $N_{\rm GC}$ within $1.5R_{\rm e}$, we assumed that half of the GC population is within $1.5R_{\rm e}$, and therefore the total population is four times the background-corrected GC density over a $1.5R_{\rm e}$ area multiplied by the area (van Dokkum et al. 2016).

To estimate the uncertainty on $N_{\rm GC}$, we combined the *rms* of the global background, the Poissonian scatter on the over-density, $(\Sigma_{\rm GC}^{\rm UDG} - \Sigma_{\rm GC}^{bkgr}) \times Area$, plus a further 20% error on the adopted scaling factors (i.e., two for $N_{\rm GC}$ at 3 and $5R_{\rm e}$, and four at $1.5R_{\rm e}$, respectively). For the $N_{\rm GC}$ values based on local background decontamination, we propagated Poissonian uncertainties for both the background and the over-density.

As a reference value, we chose the $N_{\rm GC}$ estimated within $1.5R_{\rm e}$ and locally corrected for background contamination. Table 3 reports the GC raw counts, the background-subtracted GC counts, and the completeness-corrected GC counts within this aperture, including also the counts for the UDG 32 (Iodice et al. 2021). We also obtained $N_{\rm GC}$ for two larger apertures (3 and $5R_{\rm e}$), with both types of background corrections (local and global). We present these as supplementary material, listing the $N_{\rm GC}$ measurements in Table B.1.

The values derived using the local and the global background corrections agree with each other within the quoted uncertainties. With a few exceptions, most of our galaxies have a GC over-density consistent with zero, which is independent of the background or the adopted $R_{\rm e}$ analysis radius. This is consistent with previous work by Lim et al. (2018), who also found many UDGs without GCs.

Figure 5 shows the GCLF normalized to the total area, summed over all the galaxies listed in Table 3 with $N_{\rm GC} > 0$, within $1.5R_{\rm e}$. We also plot the global and local background luminosity function (left and right panels, respectively) and the residual luminosity function (gray shaded histogram). The best Gaussian fit parameters for the locally corrected GCLF are: $\mu_{g,\rm TOM} = 25.8 \pm 0.2$ mag, $\sigma_{\rm GCLF} = 0.66 \pm 0.14$ mag. The g-band turn-over magnitude, $\mu_{g,\rm TOM}$, is consistent with the assumptions discussed above. The estimated width, $\sigma_{\rm GCLF}$, agrees nicely with the predictions by Villegas et al. (2010) for objects with total magnitude similar to ours (see their Fig. 5). Similar results are obtained when adopting the global background correction (Fig. 5, left panel). The diagram reveals several features: (*i*) the GC candidates luminosity function (blue solid line) shows the expected steep increase when going to fainter magnitude, while approaching the TOM; (*ii*) the global background has a relatively stable distribution, with larger densities toward fainter magnitudes; (*iii*) the local background luminosity function suffers from a slightly larger scatter and a higher density of sources compared to the case of the global background, which is expected because of the local contribution of ICGCs; and (*iv*) both panels reveal the presence of a residual GC over-density (gray histograms), consistent with the expected half-Gaussian shape. These results, while supporting the evidence that a small yet non-negligible GC population is found in these UDGs, highlight the need for new observational data – either spectroscopy or near-IR photometry – in order to better constrain the bulk GCs population.

[8] The factor of two correction is strictly valid if the galaxy lies at the adopted distance modulus, at $m_g^{\rm TOM} \sim 26$ mag. However, if the galaxy is in foreground or background with respect to the adopted cluster distance, the TOM would be brighter or fainter, and therefore the correction factor would be under- or overestimated, respectively.

Table 3. Globular cluster candidate numbers and their specific frequencies associated with the new UDGs and LSB galaxies in the Hydra I cluster.

Object	Raw GCs	Back. sub. GCs	$N_{\rm GC}$	S_N
UDG 13	0	−1.4	–	–
UDG 14	1	0.04	0 ± 1	0 ± 23
UDG 15	1	0.46	2 ± 3	41 ± 75
UDG 16	0	−0.33	–	–
UDG 17	1	0.73	3 ± 3	11 ± 14
UDG 18	3	2.8	11 ± 7	168 ± 153
UDG 19	0	−0.24	–	–
UDG 20	0	−0.69	–	–
UDG 21	0	−0.6	–	–
UDG 22	0	−0.24	–	–
UDG 23	0	−0.45	–	–
UDG 32	3	1.8	7 ± 4	12 ± 10
LSB 1	0	−0.42	–	–
LSB 2	0	−0.36	–	–
LSB 3	1	−0.44	–	–
LSB 4	2	1.9	8 ± 3	28 ± 16
LSB 5	0	−0.09	–	–
LSB 6	1	0.46	2 ± 1	2 ± 1
LSB 7	0	−0.63	–	–
LSB 8	0	−0.36	–	–

Notes. For each galaxy in our sample, we show the raw GC candidate counts within a $1.5R_{\rm e}$ aperture (second column), the local background-subtracted counts (third column), the completeness-corrected total GC counts ($N_{\rm GC}$, fourth column), and the respective specific frequency (last column).

5. Results

In this section, we explore the main properties we derived for all UDGs over the Hydra I cluster area, including the first 9 candidates published by Iodice et al. (2020). We focus on the two-dimensional (2D) projected distribution of the UDGs inside the cluster and on how the structural parameters and colors vary as a function of the cluster-centric projected distance. In addition, we discuss how the structural properties of the UDGs compare with those derived for the dwarf galaxies in the cluster and, in particular, for the new LSB galaxies also presented in this work. Finally, we show how the specific frequency of GCs is related to the other physical properties and to the cluster-centric distance. The implications of these results for the nature of UDGs in Hydra I cluster are discussed in Sect. 6.

5.1. Two-dimensional distribution of UDGs inside the cluster

With rigorous consideration of the van Dokkum UDG definition (van Dokkum et al. 2015), we find that the total number of UDGs within $\approx 0.4R_{\rm vir}$ of the Hydra I cluster is 21. Eleven of these are presented here, nine by Iodice et al. (2020), and UDG 32 discovered by Iodice et al. (2021) in the stellar filaments of NGC 3314A. In order to compare these counts with the UDG-abundance-halo mass relation (van der Burg et al. 2017; Janssens et al. 2019), we need to correct $N_{\rm UDG}$. To scale it up

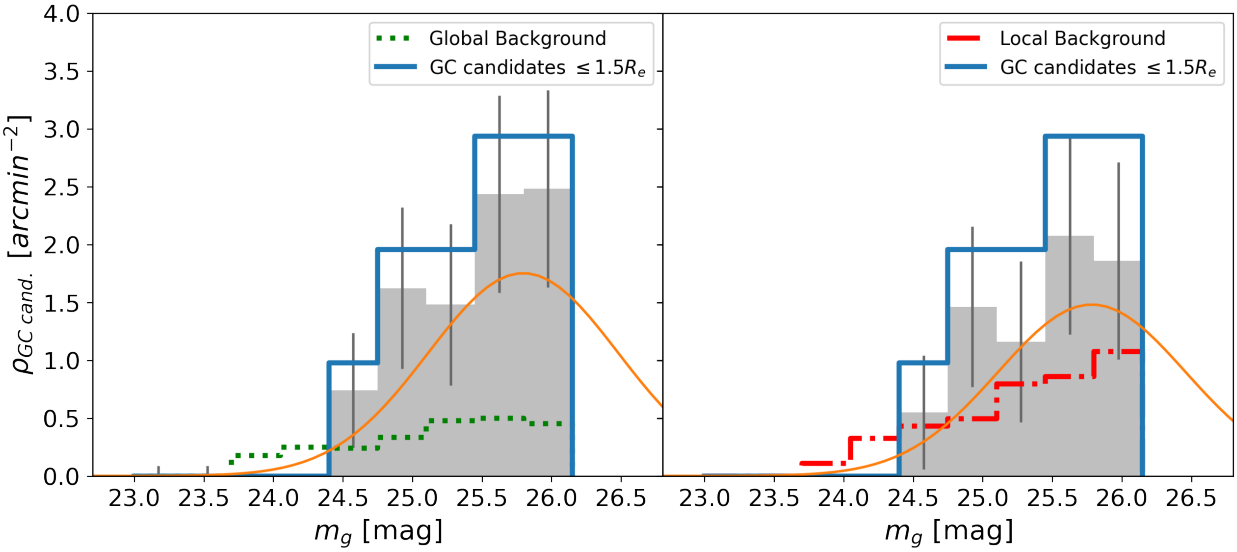

Fig. 5. Total luminosity function of the GC candidates over the joint sample of UDGs and LSB galaxies (Table 3) with $N_{GC} \geq 0$ within $1.5R_e$ normalized to the total galaxy area (solid blue line). *Left*: GCLF globally corrected. The density distribution for the global background is shown with green dotted line. The gray shaded histogram shows the residuals of the two. The solid line shows the best-fit Gaussian function of the GC luminosity function (gray bins). The best-fit parameters are: $\mu_{g,\mathrm{TOM}} = 25.8 \pm 0.3$ mag, $\sigma_{\mathrm{GCLF}} = 0.69 \pm 0.12$ mag. *Right*: As left panel, but using the local background (red dot-dashed line). The best-fit parameters are: $\mu_{g,\mathrm{TOM}} = 25.8 \pm 0.2$ mag, $\sigma_{\mathrm{GCLF}} = 0.66 \pm 0.14$ mag. The error bars show the uncertainties on the residual GC density calculated as detailed in Sect. 4.

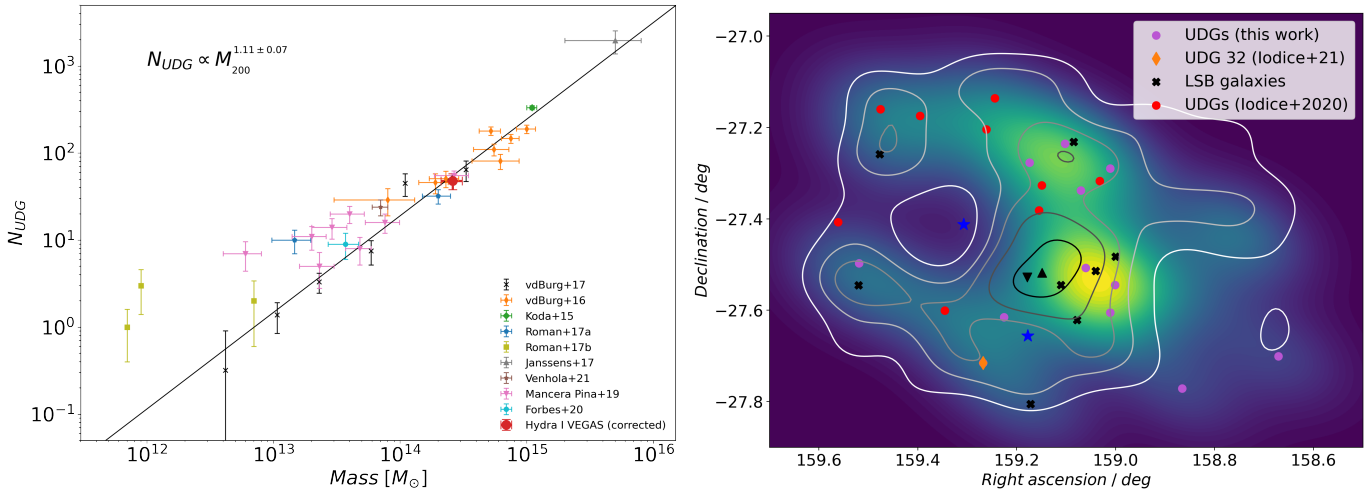

Fig. 6. UDG numerical abundance and spatial distribution. *Left panel:* abundance of UDGs as a function of the halo mass for available data (van der Burg et al. 2017, 2016; Koda et al. 2015; Román & Trujillo 2017a,b; Janssens et al. 2017; Mancera Piña et al. 2019; Forbes et al. 2020b; Venhola et al. 2022). For the Hydra I cluster, the number of UDGs within $\approx 0.4R_{\mathrm{vir}}$ is scaled to $N_{\mathrm{UDG}}(\leq R_{\mathrm{vir}})$ on an assumed radial number density distribution (see Sect. 5.1). The black line represents the relation fitted by van der Burg et al. (2017), the equation for which is reported in the plot. *Right panel:* 2D projected distribution of all the UDGs detected in the Hydra I cluster, and of the 8 LSB galaxies presented in this work (sequential color map). Contours represent the density distribution of dwarf galaxies (see Paper I), with increasing density from white to black. The two brightest cluster members NGC 3311 and NGC 3309 are marked as black triangles. The locations of the two brightest stars in the field are also indicated as blue stars.

to $1R_{\mathrm{vir}}$, we assume the radial number density distribution given by the Einasto (1965) profile fitted by van der Burg et al. (2016). As these latter authors point out, the Einasto profile provides a better description of the UDG radial density distribution than the Navarro-Frenk-White profile (Navarro et al. 1997). Therefore, we calculate the scaling number density profile factor for the Hydra I cluster based on our counts (21 UDGs within a circular area of $r = 0.4R_{\mathrm{vir}}$), and integrate the assumed number density profile on a disk of radius $1R_{\mathrm{vir}}$. We obtain 48 ± 10 UDGs for the Hydra I cluster, where the error is calculated by propagating the Poissonian error on the UDG counts. A comparison with the literature UDG abundance–halo mass relation is presented in Fig. 6 (left panel).

Figure 6 (right panel) shows the 2D spatial distribution of all 21 Hydra I UDGs detected so far, and of the 8 LSB galaxies presented here. This is obtained by convolving the galaxy distribution with a Gaussian kernel with a standard deviation of $\sigma = 5$ arcmin. The spatial distribution appears strongly asymmetric with respect to the cluster core. Most galaxies seem to be concentrated towards the cluster core and around a subgroup of galaxies to the north of it – which are the two densest regions of the cluster –, following a similar distribution found for

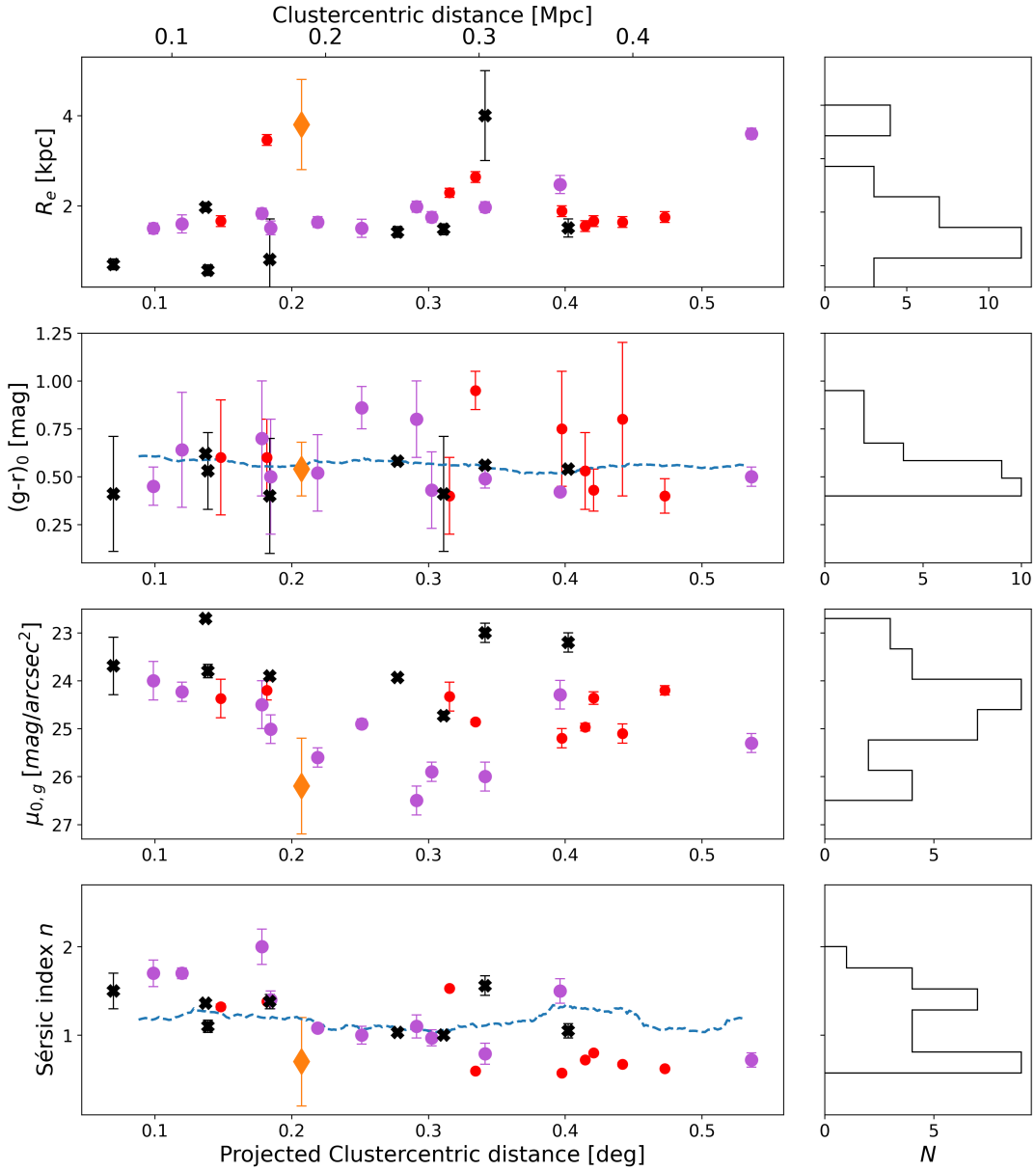

Fig. 7. *Left panel:* structural parameters for UDGs (purple circles are UDGs in this work, red circles are UDGs from Iodice et al. 2020, and the orange diamond marks UDG 32 Iodice et al. 2021) and LSB galaxies (black crosses) in the Hydra I cluster as a function of the cluster-centric projected distance. *From the top to the bottom*: effective radius R_e, $g-r$ color, central surface brightness μ_0 in the g band, and the Sérsic index n. The blue dashed line is the mean locus derived for the dwarf galaxy sample in Hydra I published in Paper I. The running mean shown is calculated considering a moving window of a fixed number of objects (50). *Right panel:* distributions of the parameters shown in the left panels.

the average dwarf galaxy population within the cluster central regions.

Like the dwarf density distribution, the 2D spatial distribution of the galaxies analyzed here presents a low density around the two brightest stars in the field. Therefore, some of the apparent asymmetries in the distribution of dwarfs (both, normal and LSB/UDGs) could be due to the presence of these two bright stars and their residual light, rather than reflecting an intrinsic physical property. For a more quantitative view of the impact of the two stars, see also the right panel of Fig. 9 in Paper I.

5.2. Cluster-centric properties

Figure 7 shows the structural parameters (R_e, μ_0, Sérsic index n) and the integrated $g-r$ color derived for each UDG as a function of the projected cluster-centric distance. For the three UDGs where we added a second component, the parameters of the outer component are taken as reference.

The effective radius peaks around 1.5 kpc, likely because of a selection effect, and does not show any trend with cluster-centric distance. However, a few UDGs have been found with larger values ($R_e \sim 2.5$ kpc). The central surface brightness spans a wide range of values at all distances from the cluster center, being $24 \leq \mu_0 \leq 27$ mag arcsec^{-2}, and also in this case, no clear trend can be seen as a function of the projected cluster-centric distance. It is worth noting that there are no UDGs fainter than $\mu_0 \geq 25$ mag arcsec^{-2} inside the angular distance of ~0.18 degrees from the cluster core. The Sérsic index n slightly increases moving inward in the cluster. Indeed, the UDGs with the highest n values are located in the innermost region of Hydra I (≤0.2 deg),

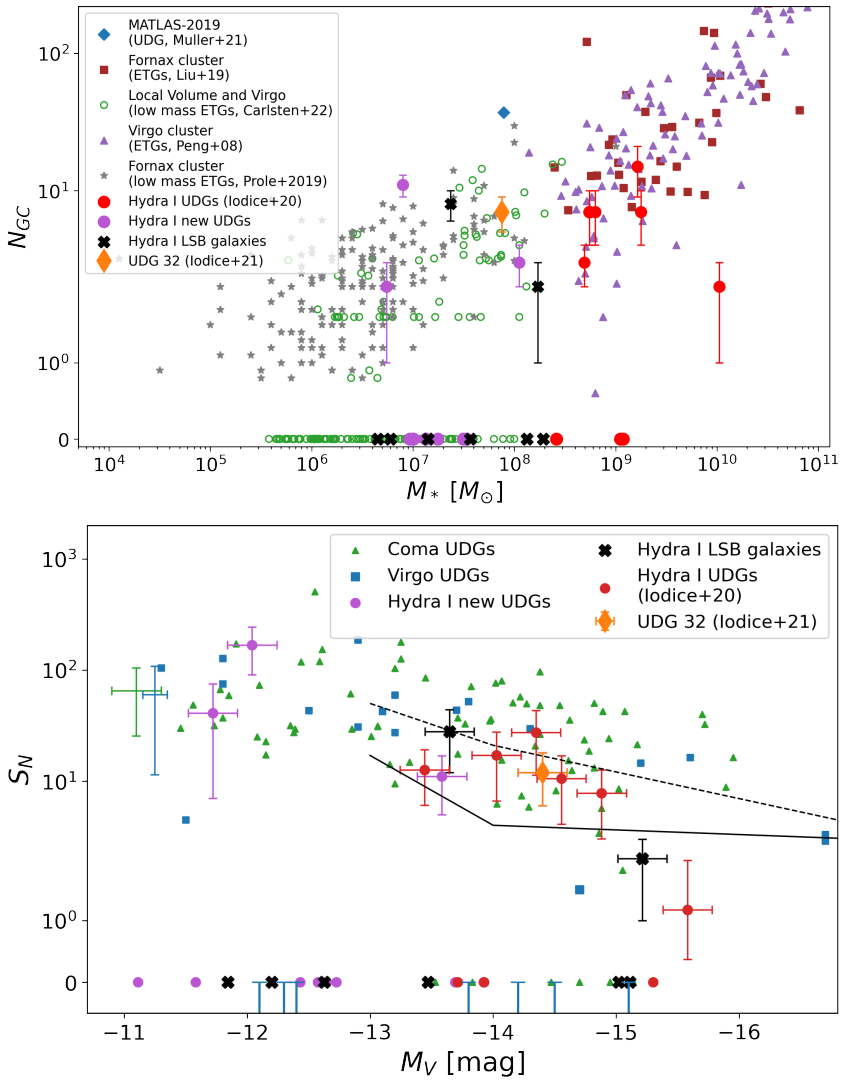

Fig. 8. *Top panel*: number of GCs as a function of the host galaxy stellar mass. Filled purple circles are the new UDGs in our sample, while filled black crosses are Hydra I new LSB galaxies. Filled red circles are Hydra I UDGs from Iodice et al. (2020), and the orange thin diamond is UDG32 (Iodice et al. 2021). High-surface-brightness and LSB galaxies from other low- and high-density environments are plotted for comparison. We show the Fornax and Virgo ETGs (Liu et al. 2019; Peng et al. 2008, respectively), the Fornax low-mass ETGs (Prole et al. 2019a), the Local Volume and Virgo low-mass ETGs (Carlsten et al. 2022), and the MATLAS-2019 UDG (Müller et al. 2021) (markers are indicated in the legend). *Bottom panel*: GC-specific frequency S_N versus V-band absolute magnitude for UDGs and new LSB galaxies in the Hydra I cluster (symbols as in the top panel, Iodice et al. 2020, and this work), compared to the UDGs in the Coma cluster (green triangles, Forbes et al. 2020a), and to the UDGs in the Virgo cluster (blue squares, Lim et al. 2020). Virgo UDGs with a negative specific frequency are reported at $S_N = 0$. In all three cases, GCs are selected within $1.5R_e$ and are locally corrected for background contamination. The solid line shows the mean locus of dwarf galaxies, the dashed line represents the upper 2σ bound (see also Fig. 4 in Lim et al. 2018). The average uncertainties on Coma and Virgo are shown on the left side.

while no UDG with $n > 1.0$ is farther than ∼0.4 deg. As a comparison, the Sérsic index n derived for the dwarf galaxies in the cluster (see Paper I) remains nearly constant at all radii, and the mean value is slightly larger (∼1) than that for UDGs (∼0.8).

The $g-r$ color of UDGs is uniformly scattered in the range ∼0.4−0.9 mag at all cluster-centric distances. These values are consistent with colors derived for the faintest red dwarf galaxies, which also do not show any trend with the distance from the cluster center (see Fig. 11 in Paper I).

5.3. Specific frequency of GCs versus physical properties

Figure 8 (top panel) shows the total number of GCs, N_{GC}, as a function of the host galaxy stellar mass, for the Hydra I LSB and UDG combined sample (both this work and Iodice et al. 2020). These are compared with galaxies in the Fornax and Virgo clusters, as well as Local Volume satellites (Liu et al. 2019; Prole et al. 2019a; Peng et al. 2008; Carlsten et al. 2022), and the UDG MATLAS-2019 (Müller et al. 2021), covering a wide range of M_* ($\sim 10^6\,M_\odot < M_* < \sim 10^{11}\,M_\odot$). The stellar masses in all these works are estimated by adopting models based on a Chabrier initial mass function (IMF, Chabrier 2003). The Into & Portinari (2013) model we adopted uses a Kroupa IMF (Kroupa 2001). However, the properties obtained using a Chabrier IMF are very similar to those obtained using a Kroupa IMF (see Fig. 4 in Bruzual & Charlot 2003). Therefore, the assumption on IMF does not affect the results shown in Fig. 8.

The GCs have been selected in apertures comparable to our choice of $1.5R_e$ by Carlsten et al. (2022) ($\leq 1.5R_e$), Müller et al. (2021) ($\leq 1.75R_e$). Prole et al. (2019a) do not put any prior on the aperture size, but they find that the typical extension of GC systems is $1.73 \pm 0.27R_e$, which is comparable to $1.5R_e$. Peng et al. (2008), Liu et al. (2019) adopt larger apertures, but their analysis is focused on much brighter galaxies.

Several low-mass galaxies in the literature have N_{GC} consistent with zero. Generally, the population of GCs increases with galaxy mass, with a larger scatter of the N_{GC} versus M_* relation in the low-mass region. Upon visual inspection, Hydra I UDGs and LSB galaxies with $N_{GC} > 0$ do not reveal substantial differences with respect to the galaxies in other environments.

For each galaxy of our new sample, $N_{GC}(\leq 1.5R_e$, local background correction) is used to derive the GC-specific frequency, $S_N = N_{GC} 10^{0.4[M_v+15]}$ (Harris & van den Bergh 1981). Results are listed in Table 3. We study the S_N as a function of the general

properties of the UDGs. As shown in the bottom panel of Fig. 8, where S_N is plotted against M_V, the values of S_N are consistent with those obtained for the previous sample of UDGs in Hydra I ($S_N \sim 5-20$, see Iodice et al. 2020) and with the average values obtained for dwarf galaxies (Lim et al. 2018). Most of the UDGs and LSB galaxies in Hydra I have a S_N consistent with that typical for dwarf galaxies of similar magnitude.

Almost half of the Hydra I UDGs (10 out of 21) have specific frequency larger than 2; in particular there are four individuals with $S_N \geq 20$. However, in all cases, the 1σ errors have the same order of magnitude of the S_N measurements, which do not allow us to draw any strong conclusion.

Hydra I UDGs and LSB galaxies seem to have S_N values comparable with Coma and Virgo UDGs (Forbes et al. 2020a; Lim et al. 2020, both works select GCs within an aperture of $1.5R_e$, using a local background correction). However, Hydra I might have a much larger fraction of UDGs with no GC over-density. Nevertheless, confirmation of this result requires new observational data, either spectroscopy or IR photometry.

To check whether the S_N distributions of UDGs for the three clusters are similar, we performed a Kolmogorov-Smirnov (KS) test (Hodges 1958), including the zero values. The p-value of the KS test gives the probability that two distributions are drawn from the same parent distribution. The three p-values are: Hydra I versus Coma: $p = 1.1 \times 10^{-8}$; Hydra I versus Virgo: $p = 0.008$; and Coma versus Virgo: $p = 0.03$. Therefore, the KS-tests indicate that the three S_N distributions are statistically different from each other. This result is substantially biased by the large number of UDGs with zero N_{GC} in our sample. Such a large fraction is likely due to the difficulties in detecting GC over-densities using g and r data for UDGs hosting less than a handful of GCs. By rejecting the UDG candidates with non-positive N_{GC} from both our Coma and Virgo cluster samples, the KS test shows that the p-values increase: Hydra I versus Coma: $p = 0.09$; Hydra I versus Virgo: $p = 0.07$; and Coma versus Virgo: $p = 0.63$. The p-values increase in all cases. Coma and Virgo S_N distributions are statistically similar with a high degree of confidence, while for the Hydra I distribution the situation is less clear. With the obtained p-values, we cannot rule out the null hypothesis that the Hydra I S_N distribution is drawn from the same parent distribution as Virgo and Coma. However, the p-values are still too low to firmly conclude that the Hydra I S_N distribution is statistically similar to those of Virgo or Coma.

In Fig. 9 we plot the S_N versus the cluster-centric distance (upper left), the $g-r$ color (upper right), the central surface brightness, and the effective radius (lower left and lower right panels, respectively). Where possible, we add the Virgo and Coma cluster UDGs.

Considering the whole sample (including the galaxies with $S_N = 0$), we cannot draw any obvious conclusion. Inspecting the galaxies with $S_N > 0$, a trend seems to be present as a function of the effective radius and of the μ_0. In particular, larger S_N values are found at smaller R_e and fainter central surface brightness. Conversely, there is no clear trend of S_N as a function of the galaxy color or of the projected cluster-centric distance. The latter finding is indirect evidence of the reliability of GC background subtraction: possible trends in S_N versus cluster-centric distance may be evidence of spurious residual contamination from ICGCs, generating false radial trends. Finally, we observe that all LSB galaxies of the combined sample with $S_N > 0$ (i.e., $N_{GC} > 0$) lie at projected cluster-centric radii of larger than 0.13 deg (~100 kpc).

6. Summary and Discussion: nature of the UDGs in the Hydra I cluster

In this paper, we present a new catalog of 19 LSB galaxies detected in the Hydra I cluster based on the VST mosaic in the g- and r- bands. Taking advantage of the large area covered and long integration times, these data allowed us to search for the LSB galaxies out to $\approx 0.4R_{vir}$, and to map the core of the cluster and the less dense regions at larger cluster-centric distances. The detection of LSB galaxies in this cluster was carried out with an automatic search using SExtractor, complemented by visual inspection, which contributed about half of the new detections.

We found 11 new UDG candidates in this sample which, adding the 9 UDGs detected by Iodice et al. (2020) and the UDG reported by Iodice et al. (2021), leads to a total number of 21 UDGs in the cluster according to the adopted UDG definition. In addition, the remaining eight galaxies of the new sample are identified as *LSB dwarfs*. Six of these latter eight are larger than the average dwarf of similar luminosity inhabiting Hydra I, with $R_e \geq 1.2$ kpc.

The 21 UDGs in Hydra I reach very faint levels of central surface brightness (down to $\mu_{0,g} \sim 26.5$ mag arcsec^{-2}), and half of them are very diffuse objects, with effective radius from ~2 to ~4 kpc. Their average $g-r$ color is in the range $0.4 \leq g-r \leq 0.9$ mag (see also Fig. 4). The stellar mass estimates we derived vary from $\sim 5 \times 10^6$ to 81.2×10^8 $M_\odot$. For all the newly detected Hydra I UDGs and LSB galaxies, we searched for compact sources around them and estimated a total GC population statistically larger than zero for 5 of the 19 newly detected galaxies (after completeness and local contamination corrections). Considering the whole Hydra I UDG population, 10 out of 21 UDGs have $N_{GC} > 0$.

The available data allowed us to derive the projected distribution of UDGs inside the covered area of the cluster and to explore the structural properties as a function of the cluster-centric distances and how they compare with the population of dwarf and newly detected LSB galaxies in the cluster. Our main results are summarized below.

1. The 2D projected distribution of UDGs and LSB galaxies seems to follow the distribution of dwarfs and giant galaxies. It appears strongly asymmetric with respect to the cluster center, although the presence of two bright stars may alter the results. Half of the UDGs (11 out of 21) are concentrated close to the cluster core and around a subgroup of galaxies to the north, which are the two densest regions of the cluster. The remaining half of the UDGs (10 objects) are found roughly uniformly distributed at larger cluster-centric distances. The LSB galaxies follow qualitatively the same projected distribution: 5 out of 8 are found in the two densest regions, while 3 are found at larger distances.
2. The average $g-r$ color of all UDGs in the sample peaks around 0.4–0.6 mag, comparable with the average colors of dwarf and LSB dwarf galaxies in the cluster. The color distribution is roughly constant with the cluster-centric distance (see Fig. 7).
3. The R_e is uniformly distributed with respect to the projected cluster-centric distance. Conversely, there is a lack of very faint UDGs ($\mu_0 \geq 25$ mag arcsec^{-2}) toward smaller cluster-centric distances (i.e., ≤0.2 deg, or ≤180 kpc), where the Sérsic index n seems to slightly increase. This trend is not observed in dwarf galaxies, where $n \sim 1$ on average at all distances (see lower panel in Fig. 7).
4. A handful of our candidates (UDG 15, UDG 17, UDG 18, UDG 32, LSB 4, and LSB 6) show a total number of GCs

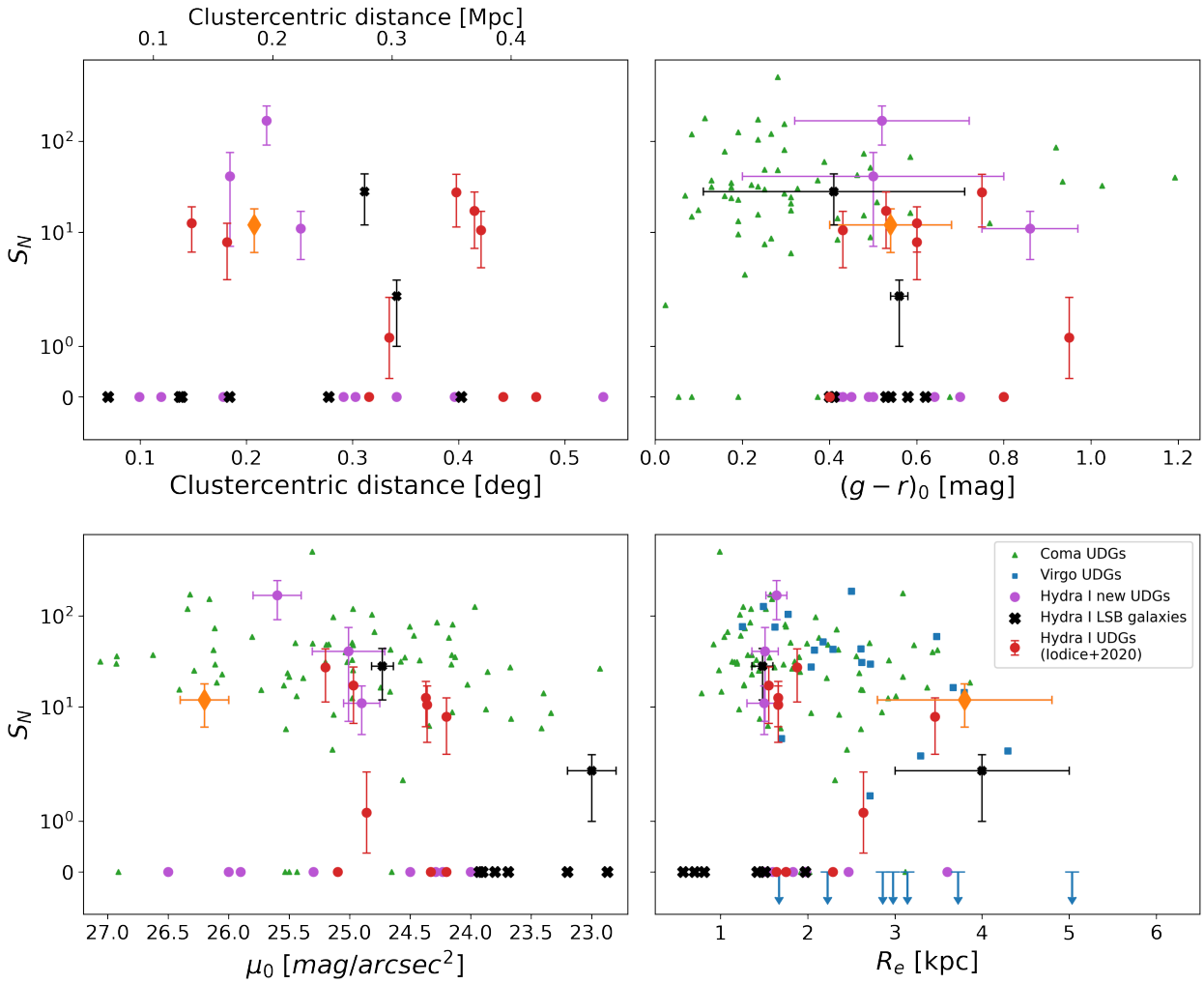

Fig. 9. GC-specific frequency S_N as a function of galaxy properties. Respectively, from left to right, and from top to bottom, S_N as a function of the cluster-centric distance, $g-r$, μ_0, and R_e. Symbols are the same as for the bottom panel of Fig. 8.

within $1.5R_e$ of larger than zero. These are consistent with the N_{GC} found in the other cluster members (Iodice et al. 2020). Considering only the Hydra I UDG candidates with $N_{GC} > 0$, the N_{GC} versus M_* relation agrees with what is found in other galaxies in the local Universe. Moreover, for the same UDGs, the GC-specific frequency is comparable with the values derived for UDGs in the Coma and Virgo clusters (Fig. 8).

We now discuss the properties and results of the UDGs in Hydra I cluster in the general framework of the nature and formation for this class of LSB galaxies. We aim to address *(i)* how the non-uniform 2D projected spatial distribution of UDGs in the cluster links to different formation scenarios; *(ii)* how UDG properties compare with those of higher-surface-brightness dwarf galaxies and the newly detected LSB galaxies in Hydra I cluster, and with UDGs in other environments (groups and clusters), and, therefore, *(iii)* whether or not different populations of UDGs exist in this cluster.

6.1. Ultra-diffuse galaxy distribution and their assembly history in Hydra I

We find that most of the UDGs are concentrated in two subgroups, one close to the cluster core and the other to the north. A similar 2D projected distribution was found for the dwarf galaxies in Hydra I (see Fig. 5 in Paper I), which peaks close to the cluster core, off-center to the NW side of the region where the BCGs are located, and to the NNW, respectively. As pointed out in Sect. 5.1, the asymmetries may also be affected by the two bright stars in the field and therefore may not accurately reflect the true bi-dimensional galaxy distribution.

All these regions are dominated by the light from the brightest cluster members. These are the two densest regions of the cluster, where there are evident signs of galaxy interactions and the presence of intra-cluster diffuse light. In a forthcoming paper, we will present clear evidence of interactions and the presence of intra-cluster LSB features inside the different subgroups of the cluster (Iodice et al. in prep.). As pointed out in Paper I, the presence of several substructures in the Hydra I cluster that emerged from the 2D distribution of dwarfs and UDGs is consistent with the previous findings by Lima-Dias et al. (2021), suggesting that this environment is still in an active assembly phase, where several subgroups of galaxies are merging into the cluster potential. In the core of the cluster, several studies reported ongoing interactions and mass assembly around NGC 3311 (see Arnaboldi et al. 2012; Hilker et al. 2018; Barbosa et al. 2018, and references therein). The spatial association of UDGs with the location of dwarf and giant galaxies in

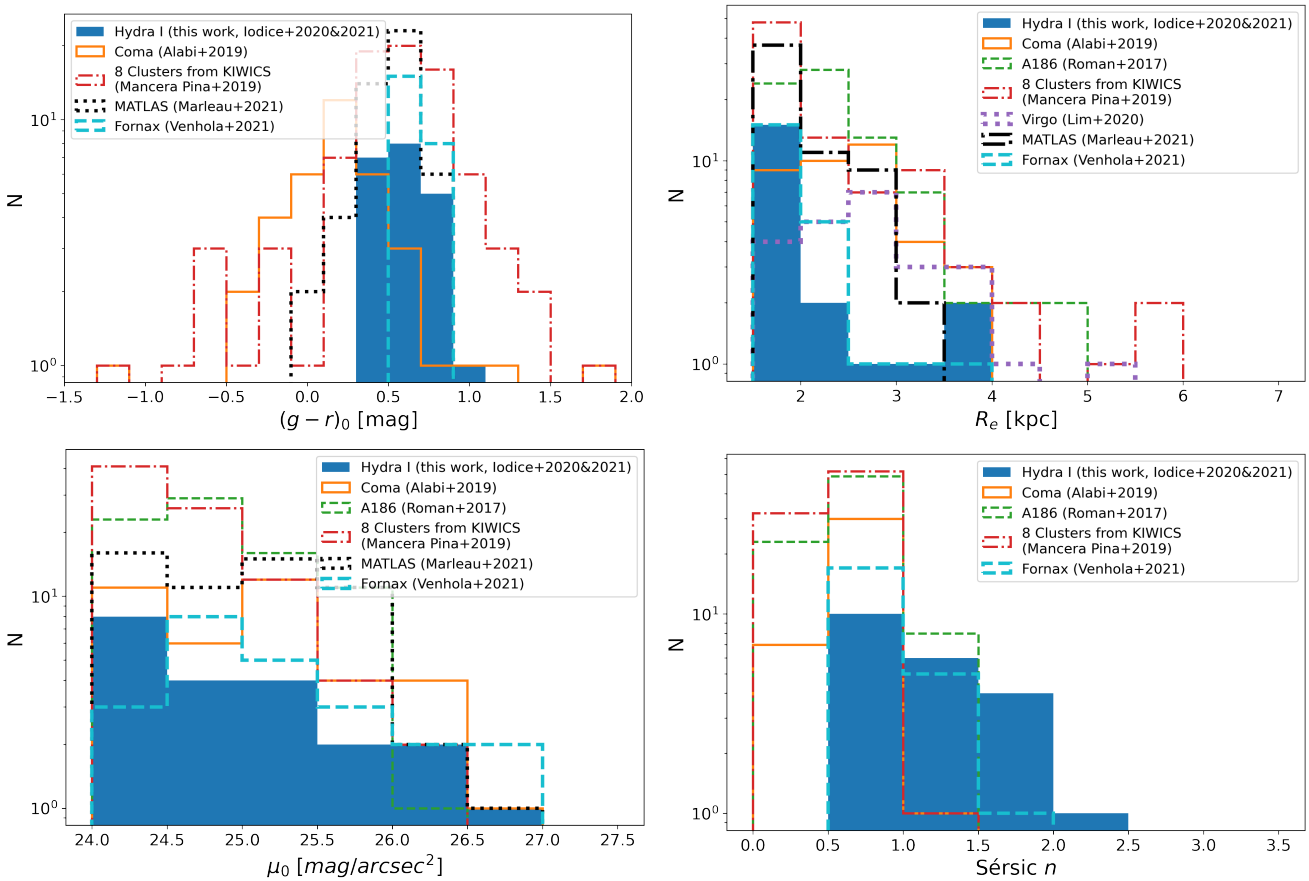

Fig. 10. Distribution of the structural parameters of UDGs in the Hydra I cluster (filled blue histogram) compared to UDGs in other environments, as listed in the legend of each panel. For each sample, we restricted the analysis to those UDGs that strictly respect the van Dokkum et al. (2015) definition. Optical $g-r$ color (*upper-left panel*), effective radius R_e (*upper-right*), central surface brightness μ_0 (*bottom-right*), and Sérsic index n (bottom-right) are compared. References are given in the legend of each panel.

the cluster is consistent with findings for other galaxy clusters, where over-densities of UDGs are found close to subgroups of galaxies (see e.g., Janssens et al. 2019). This would suggest that UDGs may be associated with groups infalling onto the cluster, which would be further evidence that UDGs join the cluster environment also via accretion of subgroups, differently from the native cluster UDGs with large DM halos, as proposed by Sales et al. (2020).

6.2. The population of UDGs in Hydra I compared to other galaxy environments

Based on their observed color distribution, it seems that two populations of UDGs exist: the red and quenched UDGs found primarily in clusters of galaxies, but also recently in low-density environments (Marleau et al. 2021), and a blue population of UDGs, which are mostly found in low-density regions (e.g., Leisman et al. 2017; Román & Trujillo 2017a; Marleau et al. 2021). In Fig. 10, we compare the Hydra I UDG property distributions with the UDGs from Fornax, Coma, and Virgo from the MATLAS survey, and from other eight nearby galaxy clusters (Venhola et al. 2022; Alabi et al. 2020; Lim et al. 2020; Marleau et al. 2021; Mancera Piña et al. 2019). For each sample, we restrict the comparison to those UDGs that rigorously respect the definition limits $R_e \geq 1.5$ kpc and $\mu_0 \geq 24$ mag arcsec^{-2}. The upper-left panel shows a comparison with the color distributions. Inside $\approx 0.4 R_{vir}$ of the Hydra I cluster, the UDGs are uniformly distributed in color, and have colors consistent with the red and quenched UDGs. It is worth noting that this result is not a selection effect, because we did not detect any blue UDG candidate that was excluded from the sample by the CMR selection. The color of the UDGs of Hydra I suggests that, at least in this studied portion of the cluster, a single population of UDGs is found. Based on the available data, we cannot exclude that bluer UDGs might exist in the outskirts of the cluster. As this population of UDGs have colors similar to the red dwarf galaxies in Hydra I and comparable stellar masses, and share the same 2D projected distribution inside the cluster, we might consider them as the extreme LSB tail of the size–luminosity distribution of dwarfs in this environment. This result might be further supported once the colors, stellar masses, and structural parameters are compared with those observed for the LSB galaxies also found in this work. These objects, which could reasonably be the largest and most diffuse dwarf galaxies in the cluster, have colors and stellar masses similar to those of the UDGs in the sample, representing the physical link between dwarfs and UDGs.

We also report that the $g-r$ color remains constant as a function of the projected cluster-centric distance. By contrast, Alabi et al. (2020) show that Coma LSB galaxies (and UDGs) have a color dependence on cluster-centric distance. Coma LSB galaxies have redder average color within the cluster core relative to the red sequence, suggesting that LSB galaxies may be most affected by the star-formation-quenching effects of the cluster-core environment. A similar color versus cluster-centric

trend was observed by Kadowaki et al. (2021). However, we point out that our data only cover the innermost portion of the Hydra I cluster ($\approx 0.4 R_{\rm vir}$), and so we cannot exclude that such a trend would appear if the population were followed further.

In the other panels of Fig. 10, the structural parameters of UDGs ($R_{\rm e}$, μ_0, n) from different clusters and less dense environments are compared (Venhola et al. 2022; Alabi et al. 2020; Mancera Piña et al. 2019; Román & Trujillo 2017a; Lim et al. 2020; Marleau et al. 2021). A general agreement is observed for the effective radius and the central surface brightness distributions. Nevertheless, a lower number of UDGs with $2.5 \leq R_{\rm e} \leq 3.5$ kpc is found in the studied portion of Hydra I. Sérsic index distributions all have similar shapes and average about $n = 1$, suggesting that UDGs in clusters are better described by exponential profiles. However, the n distribution of Hydra I shows a larger number of UDGs with Sérsic index higher than 1.5.

Inside the whole sample of UDGs and LSB galaxies, the analysis of GCs suggests that a small yet non-negligible GC population is found in these galaxies, with $N_{\rm GC} \geq 2$ within $1.5 R_{\rm e}$ for a number of galaxies (see Table B.1). Given the poor statistics, new observational data (either spectroscopy or near-IR photometry) are needed to constrain the bulk of the GC population and therefore to address the existence of a different class of UDGs in Hydra I, where large S_N might indicate a large halo mass ($>10^{10}\,M_\odot$), as found in the Coma cluster (Burkert & Forbes 2020).

7. Conclusions

In this work, we studied the main photometric properties for 19 newly detected LSB galaxies in the Hydra I cluster. Adopting the UDG definition criteria given by van Dokkum et al. (2015), 11 of the newly detected galaxies are UDG candidates, to be added to the 9 UDGs reported by Iodice et al. (2020) and the UDG in the tail of NGC3314 discovered by Iodice et al. (2021). Therefore, the total number of UDG candidates in the central region of the Hydra I cluster ($\lesssim 0.4 R_{\rm vir}$) is 21. Comparison with the high-surface brightness and LSB dwarf galaxies in this region of the cluster suggests that UDGs in this environment have similar properties. Moreover, by comparing the sample with the analogous galaxies in other environments, we observed a general agreement for $R_{\rm e}$, μ_0, and n, while a lack of blue UDGs ($g-r < 0.3$) is reported within the Hydra I cluster out to $\approx 0.4 R_{\rm vir}$ with respect to the other UDG populations (see Fig. 10).

We analyzed the GCs in each UDG. The analysis of the GC systems is hampered by the availability of only two optical passbands, which are close in terms of central wavelength, g and r. Nevertheless, the large survey area allowed us to highlight the presence of local GC over-densities by means of statistical background decontamination. A handful of our candidates show a total number of GCs, $N_{\rm GC}$, that is statistically larger than zero. However, to have more robust constraints on the GC systems in our UDG candidates, new spectroscopic or near-IR photometric data are required to further reduce GC contamination and possibly identify more UDGs with a non-zero GC population.

Thanks to the deep and wide VEGAS coverage, the Hydra I cluster offers a rare opportunity to build a complete sample of UDGs and analyze this class of LSB galaxies across the cluster density. This allows us to put constraints on the nature and formation of UDGs, also considering the wide range of parameters covered by the sample, and the existence of UDGs that differ significantly from one another in terms of GC-specific frequency. To further investigate this particular class of LSB galaxies, spectroscopic follow-up observations for the whole sample of UDGs in Hydra I will soon be available from the large programme recently approved in ESO period 108 (Run ID:108.222P), entitled Looking into the faintEst WIth muSe (LEWIS): on the nature of ultra-diffuse galaxies in the Hydra-I cluster.

Acknowledgements. We thank the anonymous referee for his/her comments and constructive suggestions. This work is based on visitor mode observations collected at the European Southern Observatory (ESO) La Silla Paranal Observatory within the VST Guaranteed Time Observations, Programme ID: 099.B-0560(A). ALM acknowledges financial support from the INAF-OAC funds. Authors acknowledge financial support from the VST INAF funds. MC acknowledges financial support from MIUR (PRIN 2017 grant 20179ZF5KS). CS is supported by an 'Hintze Fellow' at the Oxford Centre for Astrophysical Surveys, which is funded through generous support from the Hintze Family Charitable Foundation. GD acknowledges support from FONDECYT REGULAR 1200495, and ANID project Basal FB-210003. ALM wishes to thank Pavel E. Mancera Piña for providing the galaxy catalogs from his works. This research made use of Astropy, (`http://www.astropy.org`) a community-developed core Python package for Astronomy (Astropy Collaboration 2013, 2018).

References

Alabi, A. B., Romanowsky, A. J., Forbes, D. A., Brodie, J. P., & Okabe, N. 2020, MNRAS, 496, 3182
Amorisco, N. C., & Loeb, A. 2016, MNRAS, 459, L51
Arnaboldi, M., Ventimiglia, G., Iodice, E., Gerhard, O., & Coccato, L. 2012, A&A, 545, A37
Astropy Collaboration (Price-Whelan, A. M., et al.) 2018, AJ, 156, 123
Astropy Collaboration (Robitaille, T. P., et al.) 2013, A&A, 558, A33
Barbosa, C. E., Arnaboldi, M., Coccato, L., et al. 2018, A&A, 609, A78
Benavides, J. A., Sales, L. V., Abadi, M. G., et al. 2021, Nat. Astron., 5, 1255
Bennet, P., Sand, D. J., Zaritsky, D., et al. 2018, ApJ, 866, L11
Bertin, E., & Arnouts, S. 1996, A&AS, 117, 393
Binggeli, B., & Cameron, L. M. 1991, A&A, 252, 27
Bradley, L., Sipőcz, B., Robitaille, T., et al. 2020, `https://doi.org/10.5281/zenodo.4044744`
Bruzual, G., & Charlot, S. 2003, MNRAS, 344, 1000
Burkert, A., & Forbes, D. A. 2020, AJ, 159, 56
Cantiello, M., D'Abrusco, R., Spavone, M., et al. 2018a, A&A, 611, A93
Cantiello, M., Grado, A., Rejkuba, M., et al. 2018b, A&A, 611, A21
Cantiello, M., Venhola, A., Grado, A., et al. 2020, A&A, 639, A136
Carleton, T., Errani, R., Cooper, M., et al. 2019, MNRAS, 485, 382
Carleton, T., Guo, Y., Munshi, F., Tremmel, M., & Wright, A. 2021, MNRAS, 502, 398
Carlsten, S. G., Greene, J. E., Beaton, R. L., & Greco, J. P. 2022, ApJ, 927, 44
Caso, J. P., De Bórtoli, B. J., Ennis, A. I., & Bassino, L. P. 2019, MNRAS, 488, 4504
Chabrier, G. 2003, PASP, 115, 763
Christlein, D., & Zabludoff, A. I. 2003, ApJ, 591, 764
Chung, C., Yoon, S.-J., Cho, H., Lee, S.-Y., & Lee, Y.-W. 2020, ApJS, 250, 33
Collins, M. L. M., Read, J. I., Ibata, R. A., et al. 2021, MNRAS, 505, 5686
Conselice, C. J. 2018, Res. Notes Am. Astron. Soc., 2, 43
Di Cintio, A., Brook, C. B., Dutton, A. A., et al. 2017, MNRAS, 466, L1
Duc, P.-A., Paudel, S., McDermid, R. M., et al. 2014, MNRAS, 440, 1458
Einasto, J. 1965, Trudy Astrofizicheskogo Instituta Alma-Ata, 5, 87
Emsellem, E., van der Burg, R. F. J., Fensch, J., et al. 2019, A&A, 625, A76
Fensch, J., van der Burg, R. F. J., Jeřábková, T., et al. 2019, A&A, 625, A77
Ferré-Mateu, A., Alabi, A., Forbes, D. A., et al. 2018, MNRAS, 479, 4891
Forbes, D. A. 2017, MNRAS, 472, L104
Forbes, D. A., Gannon, J., Couch, W. J., et al. 2019, A&A, 626, A66
Forbes, D. A., Dullo, B. T., Gannon, J., et al. 2020a, MNRAS, 494, 5293
Forbes, D. A., Alabi, A., Romanowsky, A. J., Brodie, J. P., & Arimoto, N. 2020b, MNRAS, 492, 4874
Forbes, D. A., Gannon, J. S., Romanowsky, A. J., et al. 2021, MNRAS, 500, 1279
Gannon, J. S., Dullo, B. T., Forbes, D. A., et al. 2021, MNRAS, 502, 3144
Georgiev, I. Y., Puzia, T. H., Goudfrooij, P., & Hilker, M. 2010, MNRAS, 406, 1967
Habas, R., Marleau, F. R., Duc, P.-A., et al. 2020, MNRAS, 491, 1901
Harris, W. E., & van den Bergh, S. 1981, AJ, 86, 1627
Hilker, M., Richtler, T., Barbosa, C. E., et al. 2018, A&A, 619, A70
Hodges, J. L. 1958, Arkiv för Matematik, 3, 469
Hudson, M. J., Harris, G. L., & Harris, W. E. 2014, ApJ, 787, L5
Into, T., & Portinari, L. 2013, MNRAS, 430, 2715
Iodice, E., Cantiello, M., Hilker, M., et al. 2020, A&A, 642, A48
Iodice, E., La Marca, A., Hilker, M., et al. 2021, A&A, 652, L11

Janssens, S., Abraham, R., Brodie, J., et al. 2017, ApJ, 839, L17
Janssens, S. R., Abraham, R., Brodie, J., Forbes, D. A., & Romanowsky, A. J. 2019, ApJ, 887, 92
Jones, M. G., Bennet, P., Mutlu-Pakdil, B., et al. 2021, ApJ, 919, 72
Kadowaki, J., Zaritsky, D., Donnerstein, R. L., et al. 2021, ApJ, 923, 257
Kartha, S. S., Forbes, D. A., Spitler, L. R., et al. 2014, MNRAS, 437, 273
Koch, A., Burkert, A., Rich, R. M., et al. 2012, ApJ, 755, L13
Koda, J., Yagi, M., Yamanoi, H., & Komiyama, Y. 2015, ApJ, 807, L2
Kostov, A., & Bonev, T. 2018, Bulg. Astron. J., 28, 3
Kroupa, P. 2001, MNRAS, 322, 231
Kuijken, K. 2011, The Messenger, 146, 8
La Marca, A., Peletier, R., Iodice, E., et al. 2022, A&A, 659, A92
Lee, J. H., Kang, J., Lee, M. G., & Jang, I. S. 2020, ApJ, 894, 75
Lee, J., Shin, E.-J., & Kim, J.-H. 2021, ApJ, 917, L15
Leisman, L., Haynes, M. P., Janowiecki, S., et al. 2017, ApJ, 842, 133
Lelli, F., Duc, P.-A., Brinks, E., et al. 2015, A&A, 584, A113
Lim, S., Peng, E. W., Côté, P., et al. 2018, ApJ, 862, 82
Lim, S., Côté, P., Peng, E. W., et al. 2020, ApJ, 899, 69
Lima-Dias, C., Monachesi, A., Torres-Flores, S., et al. 2021, MNRAS, 500, 1323
Liu, Y., Peng, E. W., Jordán, A., et al. 2019, ApJ, 875, 156
Mancera Piña, P. E., Peletier, R. F., Aguerri, J. A. L., et al. 2018, MNRAS, 481, 4381
Mancera Piña, P. E., Aguerri, J. A. L., Peletier, R. F., et al. 2019, MNRAS, 485, 1036
Marleau, F. R., Habas, R., Poulain, M., et al. 2021, A&A, 654, A105
Martín-Navarro, I., Romanowsky, A. J., Brodie, J. P., et al. 2019, MNRAS, 484, 3425
Merritt, A., van Dokkum, P., Danieli, S., et al. 2016, ApJ, 833, 168
Mihos, J. C., Harding, P., Feldmeier, J., & Morrison, H. 2005, ApJ, 631, L41
Misgeld, I., Mieske, S., & Hilker, M. 2008, A&A, 486, 697
Montes, M., Infante-Sainz, R., Madrigal-Aguado, A., et al. 2020, ApJ, 904, 114
Müller, O., Rich, R. M., Román, J., et al. 2019, A&A, 624, L6
Müller, O., Marleau, F. R., Duc, P.-A., et al. 2020, A&A, 640, A106
Müller, O., Durrell, P. R., Marleau, F. R., et al. 2021, ApJ, 923, 9
Navarro, J. F., Frenk, C. S., & White, S. D. M. 1997, ApJ, 490, 493
Pandya, V., Romanowsky, A. J., Laine, S., et al. 2018, ApJ, 858, 29
Peng, E. W., Jordán, A., Côté, P., et al. 2008, ApJ, 681, 197
Peng, E. W., Ferguson, H. C., Goudfrooij, P., et al. 2011, ApJ, 730, 23
Ploeckinger, S., Sharma, K., Schaye, J., et al. 2018, MNRAS, 474, 580
Poggianti, B. M., Gullieuszik, M., Tonnesen, S., et al. 2019, MNRAS, 482, 4466
Prole, D. J., van der Burg, R. F. J., Hilker, M., & Davies, J. I. 2019a, MNRAS, 488, 2143
Prole, D. J., Hilker, M., van der Burg, R. F. J., et al. 2019b, MNRAS, 484, 4865
Rejkuba, M. 2012, Ap&SS, 341, 195
Richter, O. G. 1987, A&AS, 67, 237
Richter, O. G., Materne, J., & Huchtmeier, W. K. 1982, A&A, 111, 193
Román, J., & Trujillo, I. 2017a, MNRAS, 468, 703
Román, J., & Trujillo, I. 2017b, MNRAS, 468, 4039
Román, J., Beasley, M. A., Ruiz-Lara, T., & Valls-Gabaud, D. 2019, MNRAS, 486, 823
Rong, Y., Guo, Q., Gao, L., et al. 2017, MNRAS, 470, 4231
Saifollahi, T., Trujillo, I., Beasley, M. A., Peletier, R. F., & Knapen, J. H. 2021, MNRAS, 502, 5921
Saifollahi, T., Zaritsky, D., Trujillo, I., et al. 2022, MNRAS, 511, 4633
Sales, L. V., Navarro, J. F., Peñafiel, L., et al. 2020, MNRAS, 494, 1848
Schlafly, E. F., & Finkbeiner, D. P. 2011, ApJ, 737, 103
Sérsic, J. L. 1963, Boletin de la Asociacion Argentina de Astronomia La Plata Argentina, 6, 41
Silk, J. 2019, MNRAS, 488, L24
Springel, V., White, S. D. M., Jenkins, A., et al. 2005, Nature, 435, 629
Tamura, T., Makishima, K., Fukazawa, Y., Ikebe, Y., & Xu, H. 2000, ApJ, 535, 602
Toloba, E., Lim, S., Peng, E., et al. 2018, ApJ, 856, L31
Tremmel, M. J., Wright, A., Munshi, F., et al. 2019, Am. Astron. Soc. Meeting Abstr., 233, 416.04
Tremmel, M., Wright, A. C., Brooks, A. M., et al. 2020, MNRAS, 497, 2786
Trujillo, I., Roman, J., Filho, M., & Sánchez Almeida, J. 2017, ApJ, 836, 191
van der Burg, R. F. J., Muzzin, A., & Hoekstra, H. 2016, A&A, 590, A20
van der Burg, R. F. J., Hoekstra, H., Muzzin, A., et al. 2017, A&A, 607, A79
van Dokkum, P. G., Romanowsky, A. J., Abraham, R., et al. 2015, ApJ, 804, L26
van Dokkum, P., Abraham, R., Brodie, J., et al. 2016, ApJ, 828, L6
van Dokkum, P., Danieli, S., Cohen, Y., et al. 2018, Nature, 555, 629
van Dokkum, P., Wasserman, A., Danieli, S., et al. 2019, ApJ, 880, 91
Venhola, A., Peletier, R., Laurikainen, E., et al. 2017, A&A, 608, A142
Venhola, A., Peletier, R. F., Salo, H., et al. 2022, A&A, 662, A43
Villegas, D., Jordán, A., Peng, E. W., et al. 2010, ApJ, 717, 603
Wright, A. C., Tremmel, M., Brooks, A. M., et al. 2021, MNRAS, 502, 5370
Yagi, M., Koda, J., Komiyama, Y., & Yamanoi, H. 2016, ApJS, 225, 11
Zaritsky, D., Donnerstein, R., Dey, A., et al. 2019, ApJS, 240, 1

Appendix A: An example of GC detection in UDGs

In section 4 we explain the details of how we select GC candidates around each UDG. Here we present the selection cuts for an example galaxy, namely UDG 13. In Figure A.1 we show the following g-band cuts: *(i)* magnitude $23.5 \geq m_g \geq 26.0$ mag; *(ii)* color $0.25 \leq g - r \leq 1.25$ mag; *(iii)* SExtractor star/galaxy classifier $CLASS\_STAR \geq 0.4$; *(iv)* concentration index CI_g within ±0.1 mag of the local sequence of point sources; and *(v)* location selection, i.e., within 1.5, 3, 5 R_e. For sake of clarity, we do not show the elongation selection, which is the least constraining criterion in our procedure.

In Figure A.1 we report all the detected objects and specifically mark the likely MW stars, the GC candidates in the analyzed cutout, and those that are within $5R_e$ from the galaxy center.

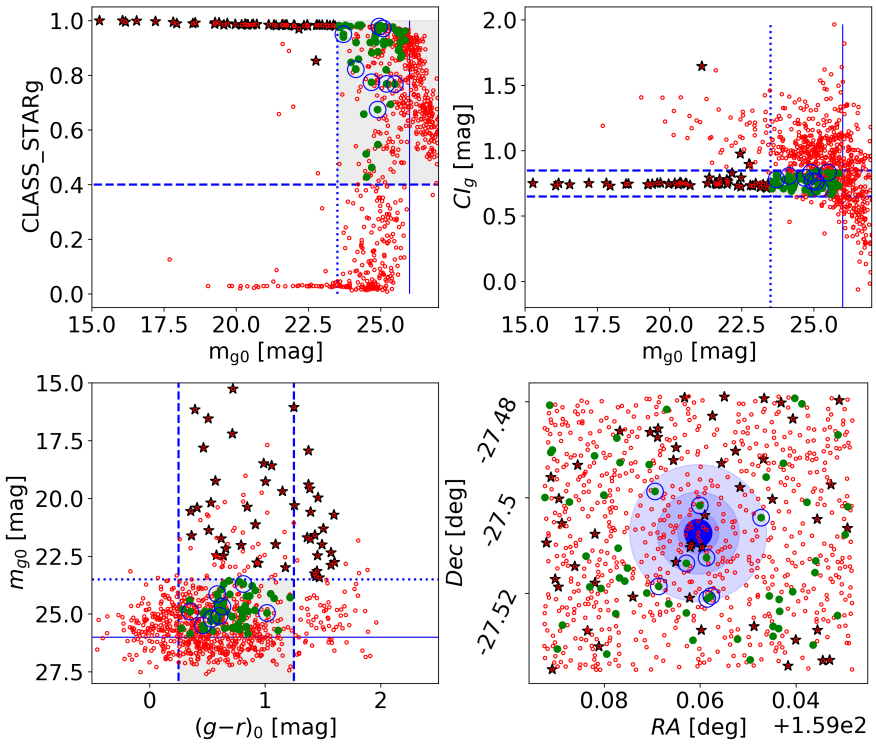

Fig. A.1. Globular cluster selection process and cuts for UDG 13. Red dots are all the sources detected in the $20R_e \times 20R_e$ cutout centered on the galaxy. The green filled dots are all the sources matching the GC selection criteria described in Sec. 4. The blue empty circles around the green filled dots identify GC candidates within $5R_e$ of the UDG. Black-filled five-pointed stars mark bright point sources, likely MW stars. *Upper left*: g-band CLASS_STAR vs. magnitude. The thin solid blue line at 26 mag represents the TOM, the blue dotted line is the the $3\sigma_{GCLF}$ brighter selection cut. The horizontal blue dashed line shows the adopted star/galaxy cut. *Upper right:* g-band concentration index CI vs. magnitude. Vertical lines are the same as the upper left panel, while horizontal blue dashed lines show the ±0.1 mag region around the local CI_g sequence of point sources. *Bottom left*: Color–magnitude diagram. The dashed blue lines show the $0.25 \leq (g - r)_0 \leq 1.25$ mag color cut. The other lines are as in previous panels. *Bottom right* : UDG 13 cutout field. Concentric shaded blue circles represent the 1, 1.5, 3, and 5 R_e regions.

Appendix B: N_{GC} and S_N within the other apertures

In this Appendix we present the GC counts within 3 and 5 R_e, for both new LSB dwarfs and UDGs in our sample. We show both the global and local corrected numbers, and the respective specific frequency. Additionally, we list the globally corrected N_{GC} within 1.5 R_e aperture radius. We include the GC counts for the UDG 32 presented by Iodice et al. (2021). Values are reported in Table B.1.

Table B.1. Globular clusters and associated specific frequencies of the new UDG candidates in the Hydra I cluster.

Object	Global determination						Local determination			
	N_{GC}			S_N			N_{GC}		S_N	
	1.5 R_e	3 R_e	5 R_e	1.5 R_e	3 R_e	5 R_e	3 R_e	5 R_e	3 R_e	5 R_e
UDG 13	-	-	-	-	-	-	-	1 ± 9	-	11 ± 100
UDG 14	-	4 ± 3	1 ± 5	-	93 ± 93	23 ± 131	4 ± 6	3 ± 9	93 ± 170	70 ± 233
UDG 15	2 ± 1	-	-	41 ± 36	-	-	-	-	-	-
UDG 16	-	-	-	-	-	-	-	-	-	-
UDG 17	3 ± 1	-	-	11 ± 7	-	-	-	-	-	-
UDG 18	11 ± 4	5 ± 2	7 ± 3	195 ± 108	76 ± 52	107 ± 78	7 ± 7	10 ± 10	107 ± 136	153 ± 96
UDG 19	-	-	-	-	-	-	-	-	-	-
UDG 20	-	-	-	-	-	-	-	-	-	-
UDG 21	-	-	-	-	-	-	-	-	-	-
UDG 22	-	1.0 ± 0.4	-	-	3 ± 2	-	-	-	-	-
UDG 23	-	-	-	-	-	-	-	-	-	-
UDG 32	7 ± 3	1 ± 3	-	12 ± 8	2 ± 5	-	3 ± 5	4 ± 10	5 ± 10	7 ± 19
LSB 1	-	2 ± 1	3 ± 3	-	26 ± 26	40 ± 54	3 ± 5	5 ± 8	40 ± 79	66 ± 127
LSB 2	-	-	-	-	-	-	-	-	-	-
LSB 3	-	3 ± 3	-	-	55 ± 81	-	4 ± 7	2 ± 10	73 ± 151	36 ± 194
LSB 4	7 ± 3	3 ± 1	3 ± 1	24 ± 17	10 ± 7	10 ± 8	3 ± 5	3 ± 6	10 ± 21	10 ± 24
LSB 5	-	-	-	-	-	-	-	-	-	-
LSB 6	2 ± 1	5 ± 2	4 ± 3	2 ± 1	4 ± 2	3 ± 3	4 ± 6	2 ± 7	3 ± 6	2 ± 6
LSB 7	-	-	-	-	-	-	-	-	-	-
LSB 8	-	-	-	-	-	-	-	-	-	-

Notes. N_{GCs} listed are all corrected for background contamination. Values corrected for the global and local contamination are reported on the left and right columns, respectively.

Appendix C: Images and surface brightness distribution of 12 new UDGs

Here we present the individual images for the new UDG candidates, side by side with their surface brightness profiles in the g-band (Fig. C.1 to Fig. C.4). The best fit of a single Sérsic profile is overlaid to each profile. In Fig. C.5 and Fig. C.6 we show the growth curves for each UDG, derived from the isophote fitting. In each panel we have included the effective radius derived as the distance from the galaxy center that includes half of the total flux. This value can be easily compared with the R_e derived from the 1D fit of the surface brightness profile, listed in Tab. 1 and also shown in Fig. C.1 to Fig. C.4.

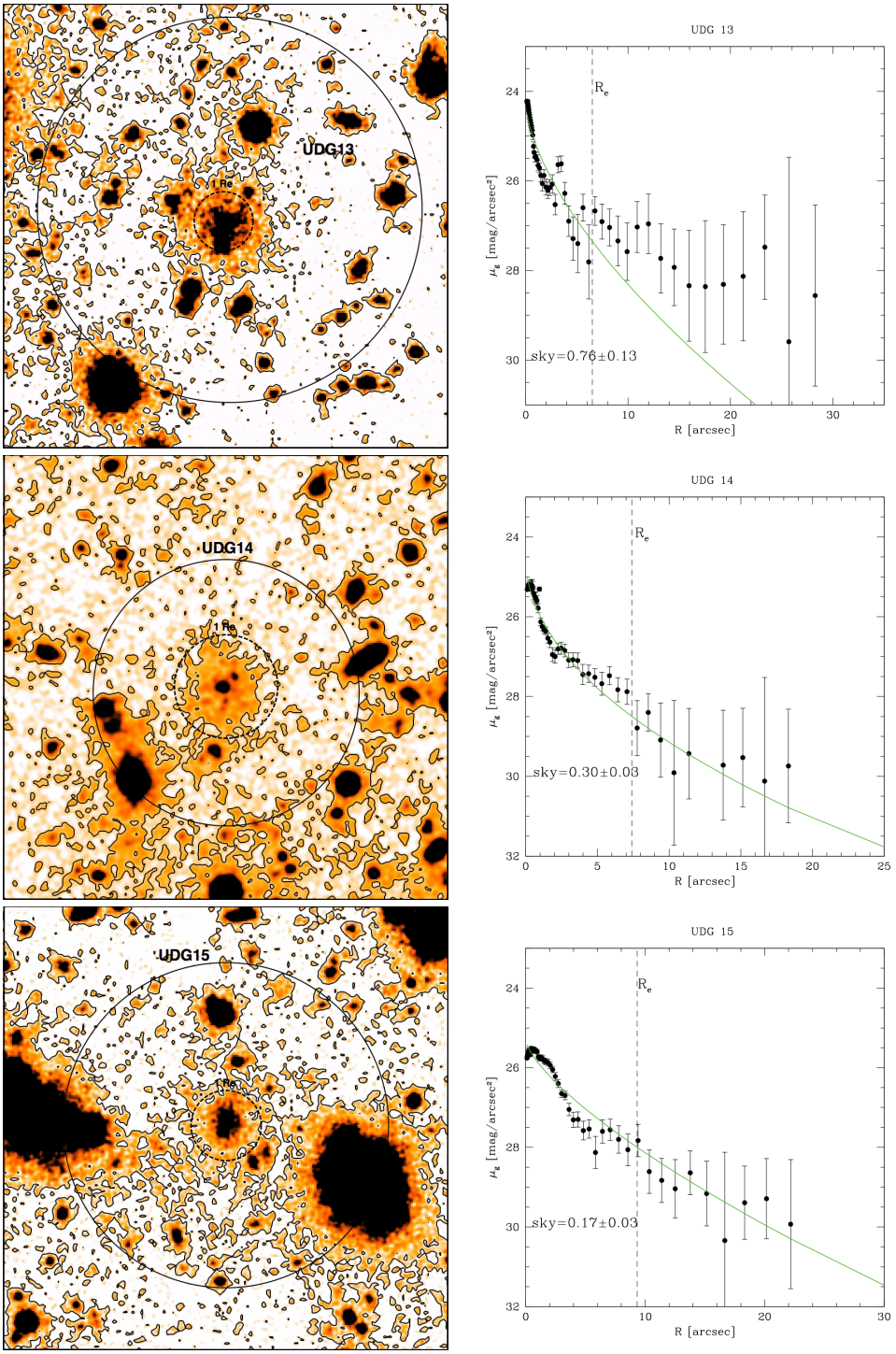

Fig. C.1. Light distribution of the UDG candidates in the g band. Left panel: Image thumbnail centered on the UDG of 1×1 arcmin ($\sim$ 14.9 kpc). The black dashed circle corresponds to $1R_e$, listed in Tab. 1. The black solid circle marks the outermost radius where flux blends into the sky level. This corresponds to the outermost data point shown in the plot in the right panel. The black solid contours correspond to $\mu_g = 29$ mag/arcsec^2. Right panel: Azimuthally averaged surface brightness profile (black points) of the UDG shown in the left panel as a function of the semi-major axis radius, and the best-fit model (green solid line). The vertical dashed line indicates the effective radius derived from the best-fit model. The local sky level (in counts) is reported in the lower-left corner of the plot.

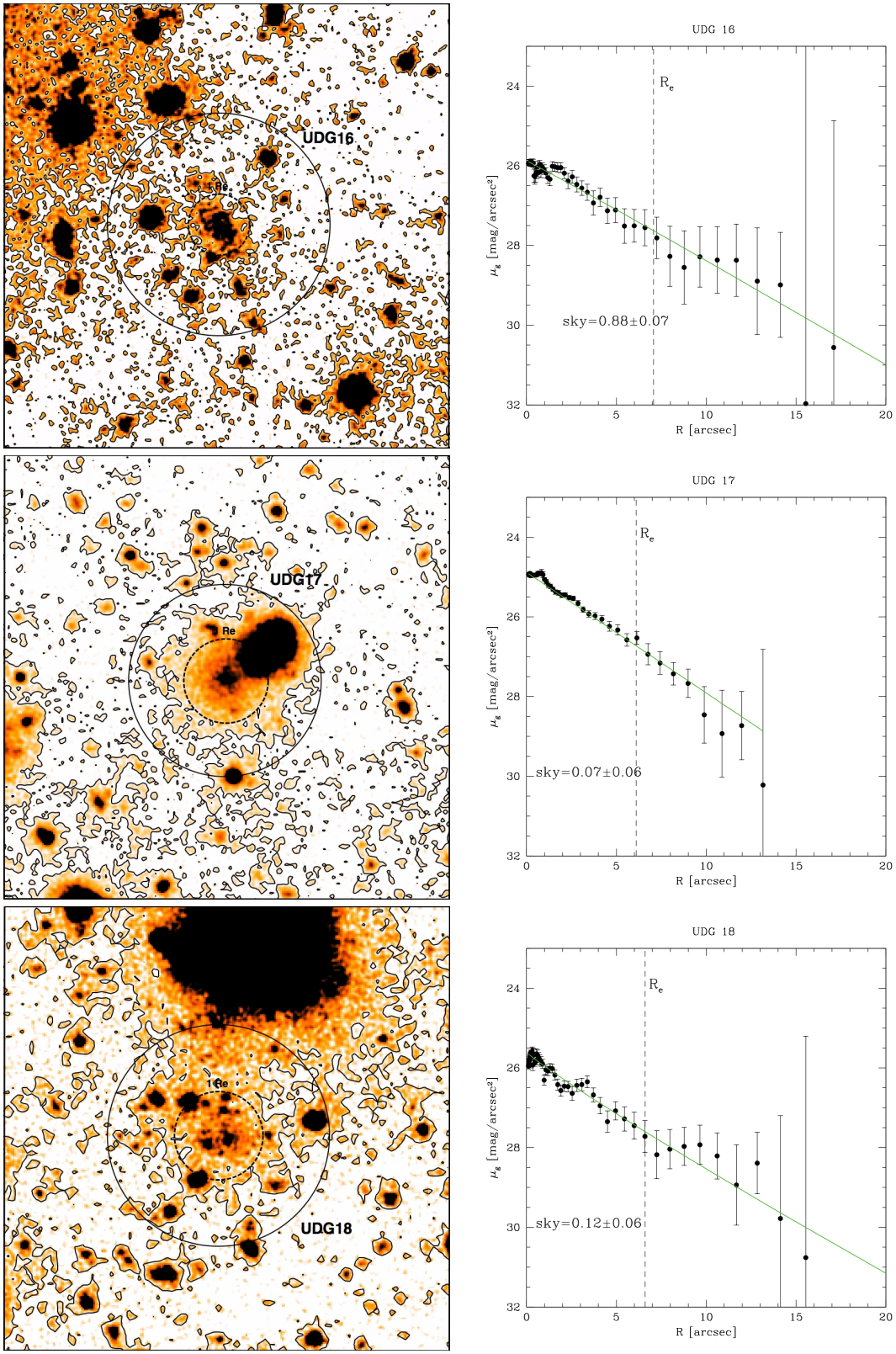

Fig. C.2. Same as Fig. C.1 for UDG 16, UDG 17 and UDG 18.

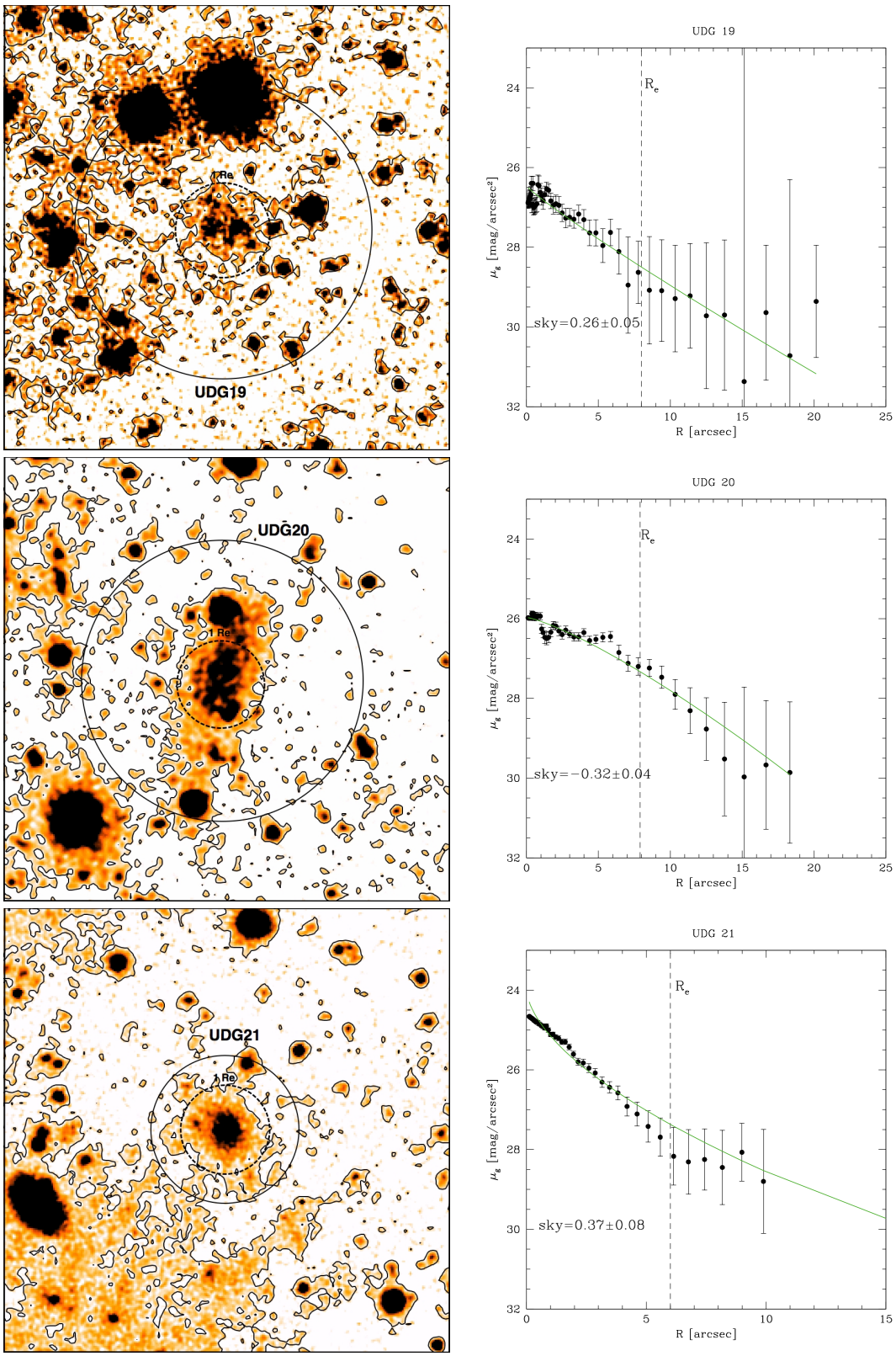

Fig. C.3. Same as Fig. C.1 for UDG 19, UDG 20 and UDG 21.

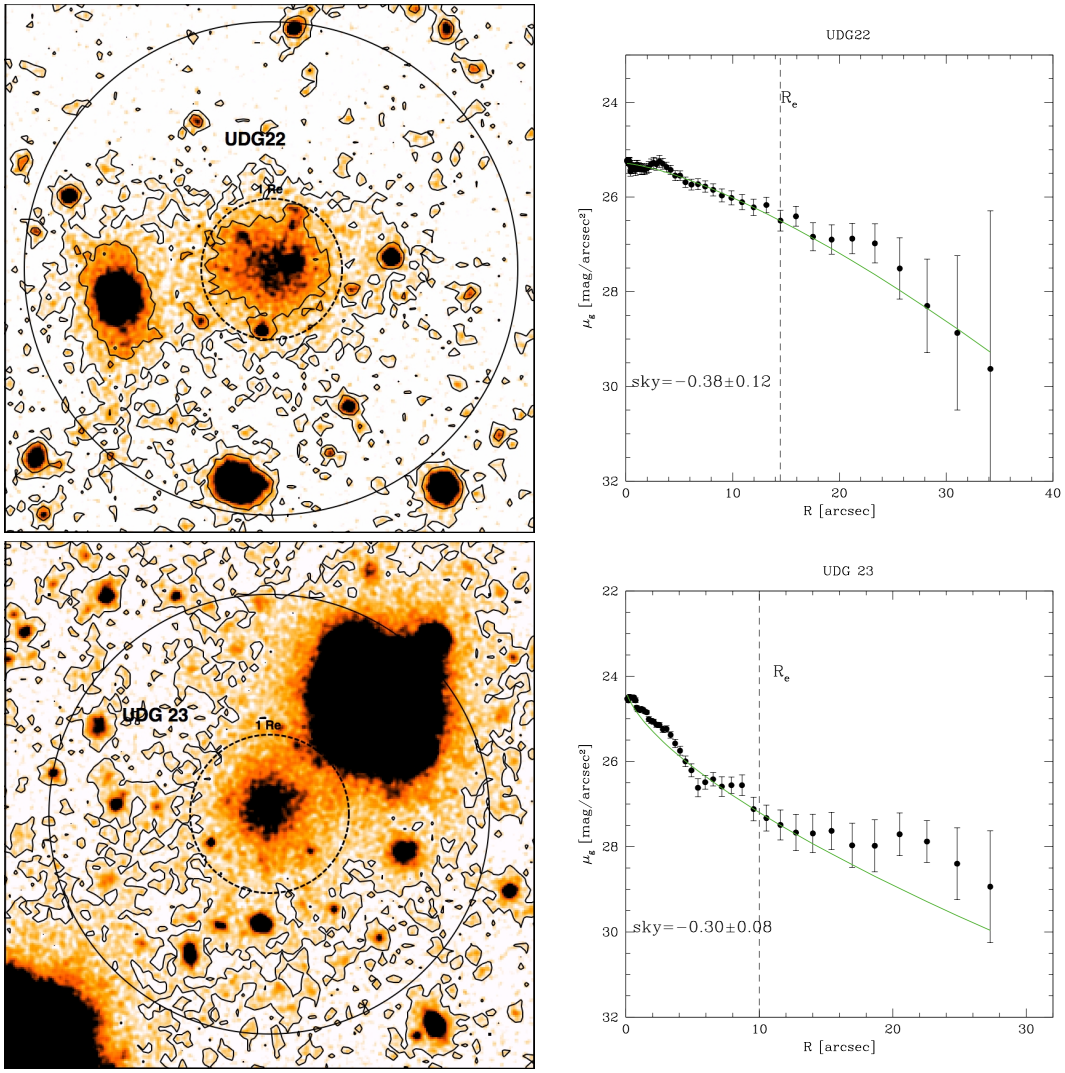

Fig. C.4. Same as Fig. C.1 for UDG 22 and UDG 23. For UDG22, we also include the contour surface brightness level corresponding to μ_e = 26.50 mag/arcsec^2; see also Tab. 1.

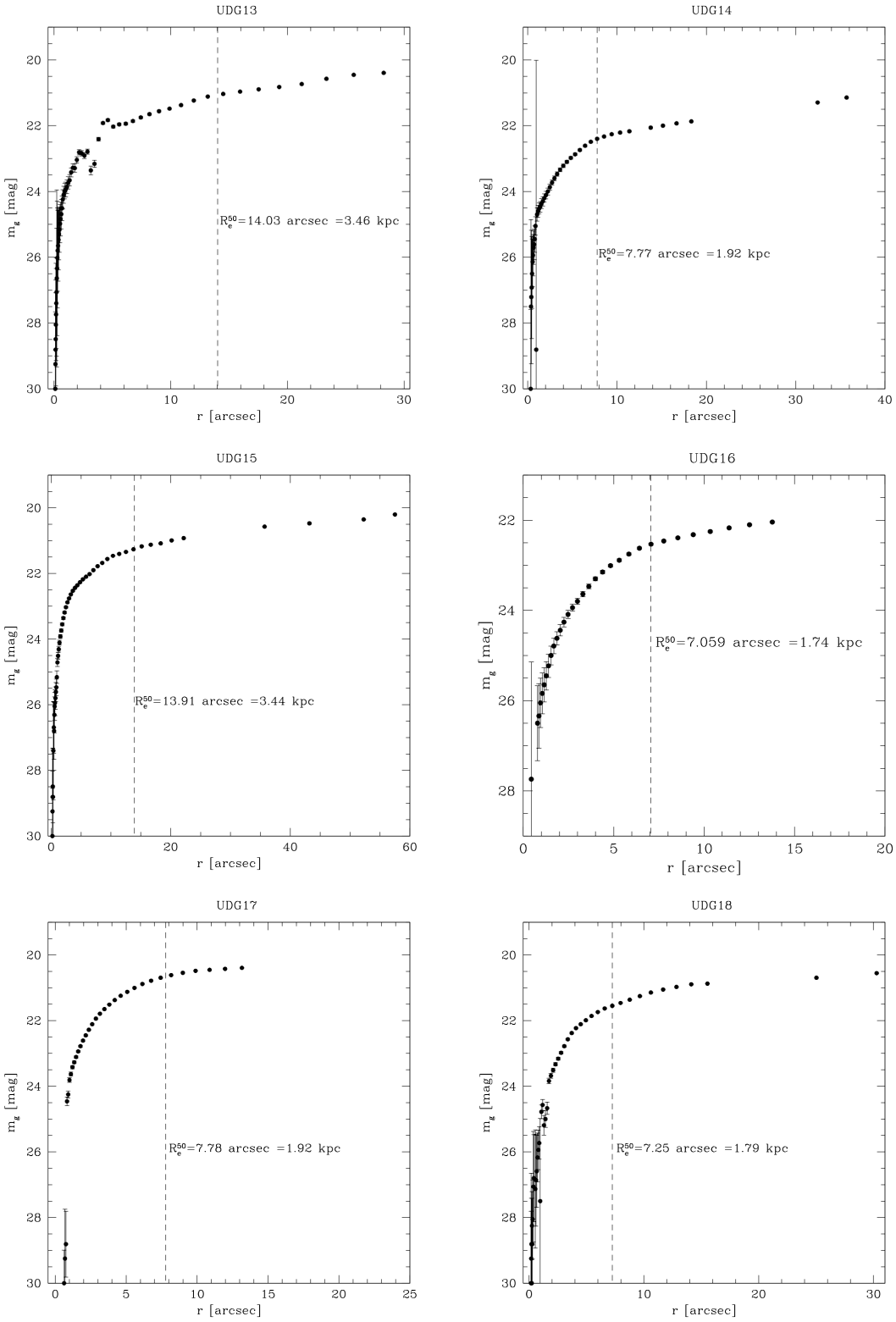

Fig. C.5. Growth curves for UDG candidates in the *g* band. Integrated magnitudes are computed from the integrated fluxes given by the isophote fits (see Sec. 3 for details). The vertical dashed line indicates the semi-major half-light radius R_e^{50}.

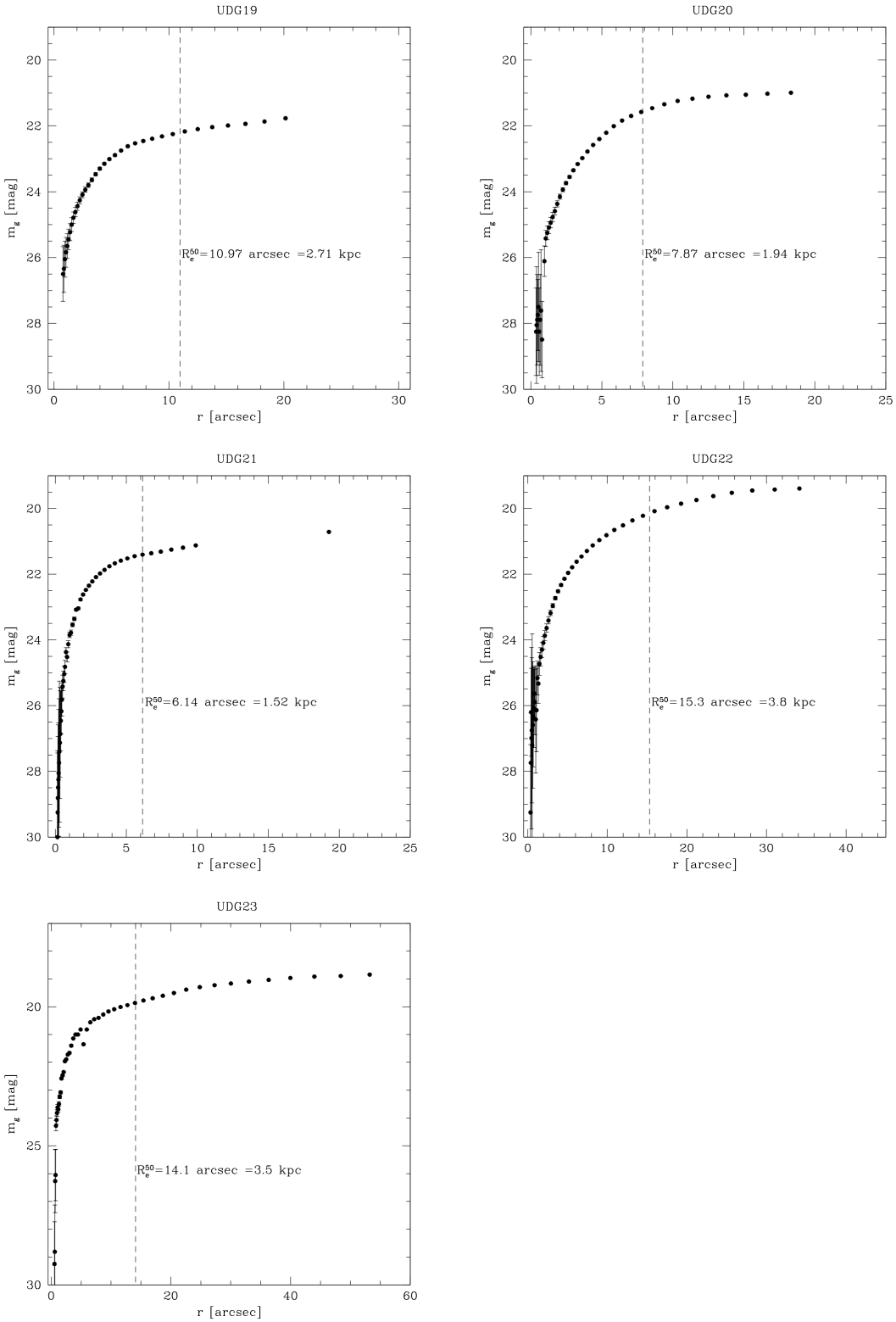

Fig. C.6. Same as Fig. C.5 for UDG 19, UDG 20, UDG 21, UDG 22, and UDG 23.

Appendix D: Images and surface brightness profiles of 8 new LSB galaxies

Here we present the individual images for the 8 new LSB galaxies (see Sec. 3), side by side with their surface brightness profiles in the g-band (Fig. D.1 to Fig. D.3). As done for the UDGs in the sample, in Fig. D.4 and Fig. D.5 we show the growth curves for each LSB galaxy, derived from the isophote fitting, where we also indicate the effective radius derived as the distance from the galaxy center that includes half of the total flux.

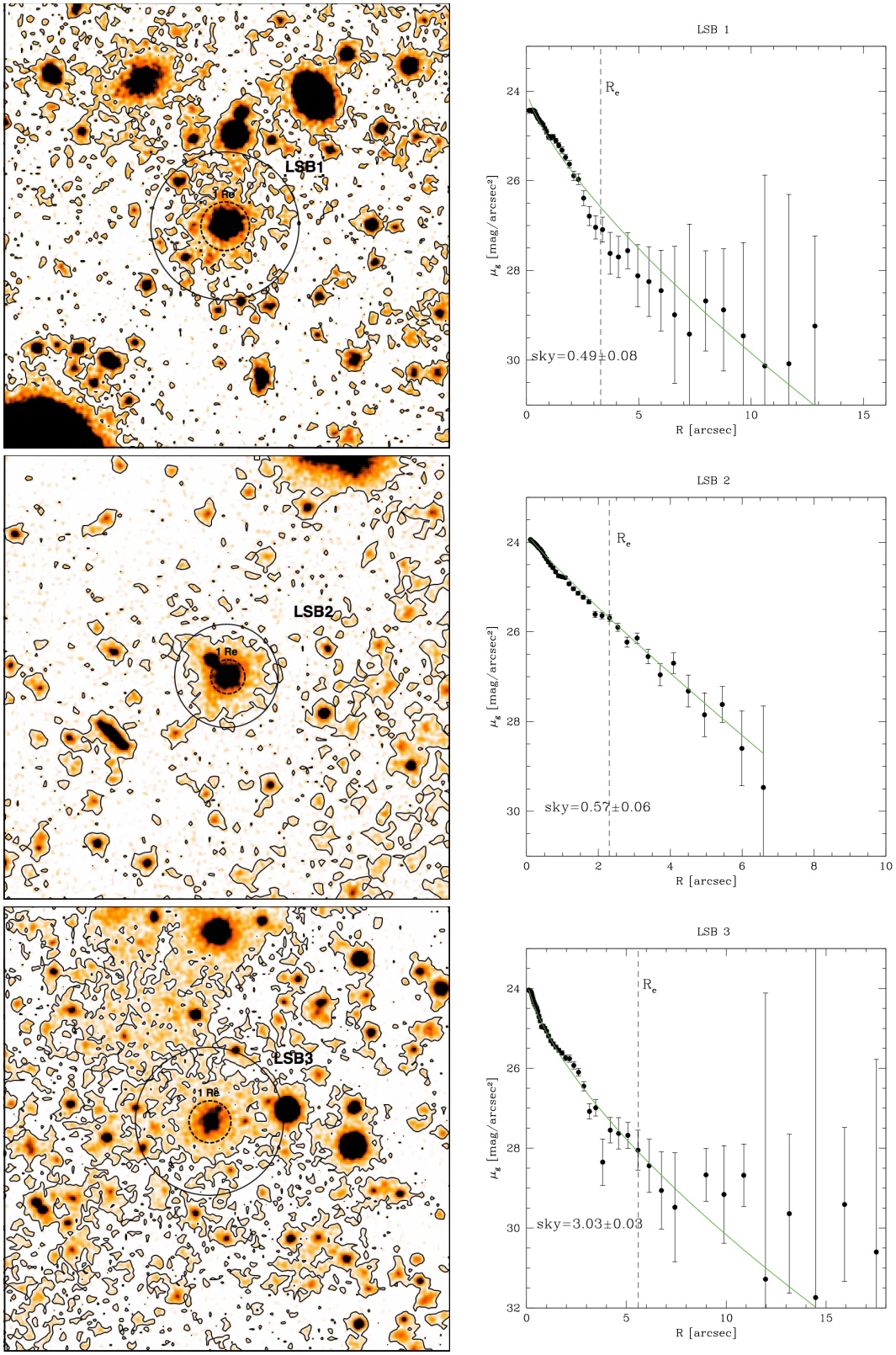

Fig. D.1. Same as Fig. C.1, for the LSB galaxies LSB 1, LSB 2, and LSB 3.

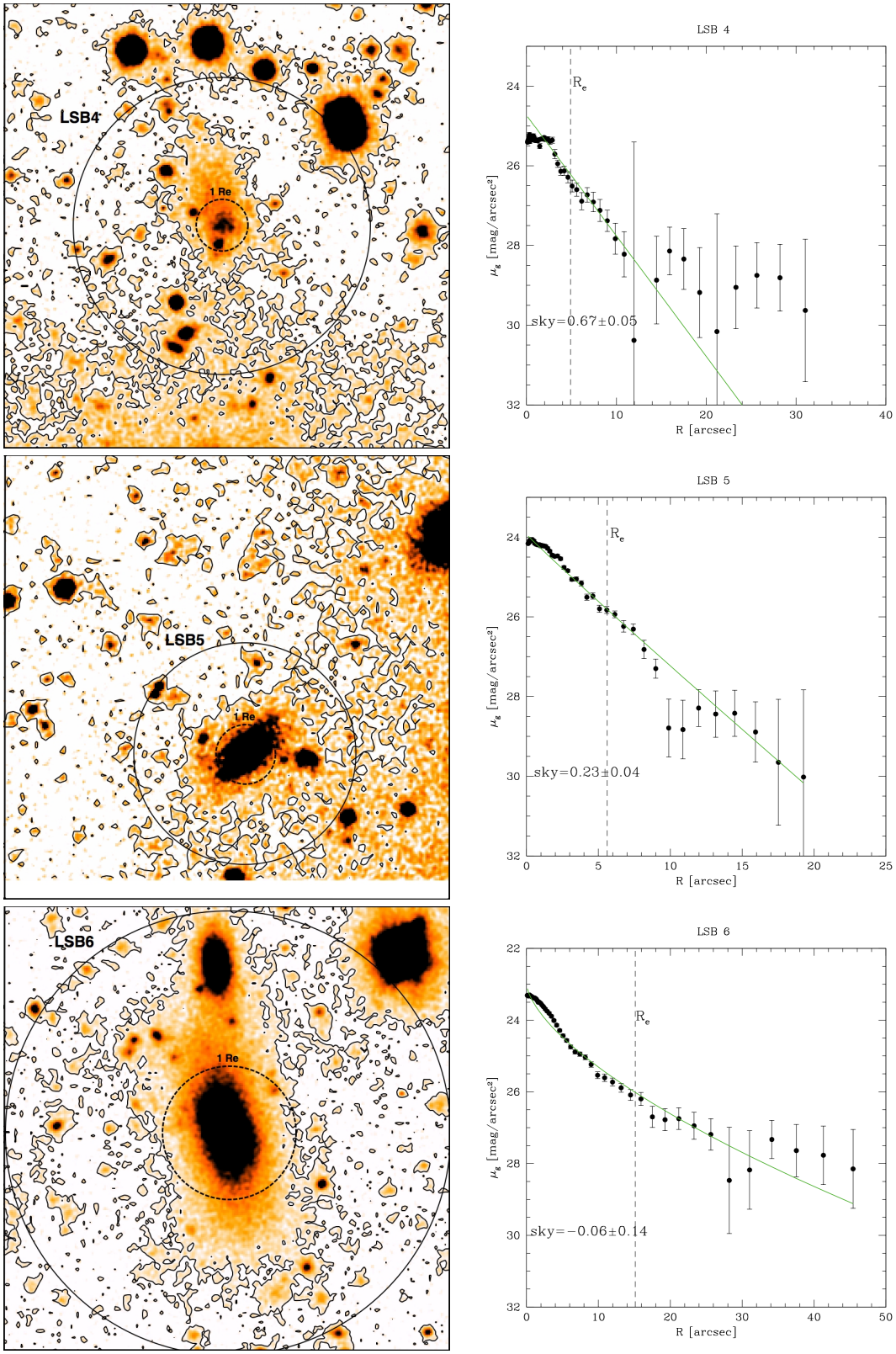

Fig. D.2. Same as Fig. D.1 for LSB 4, LSB 5, and LSB 6.

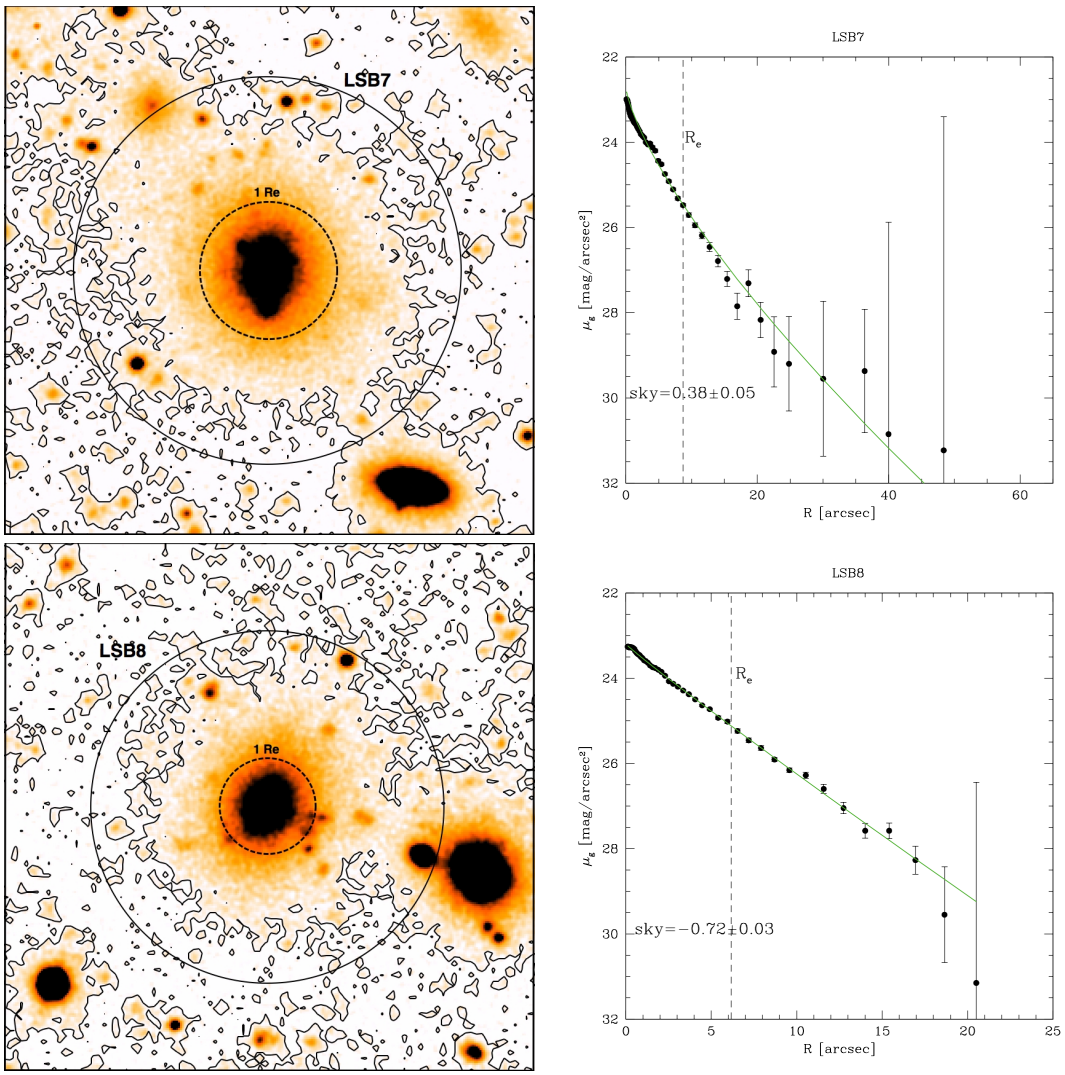

Fig. D.3. Same as Fig. D.1 for LSB 7 and LSB 8.

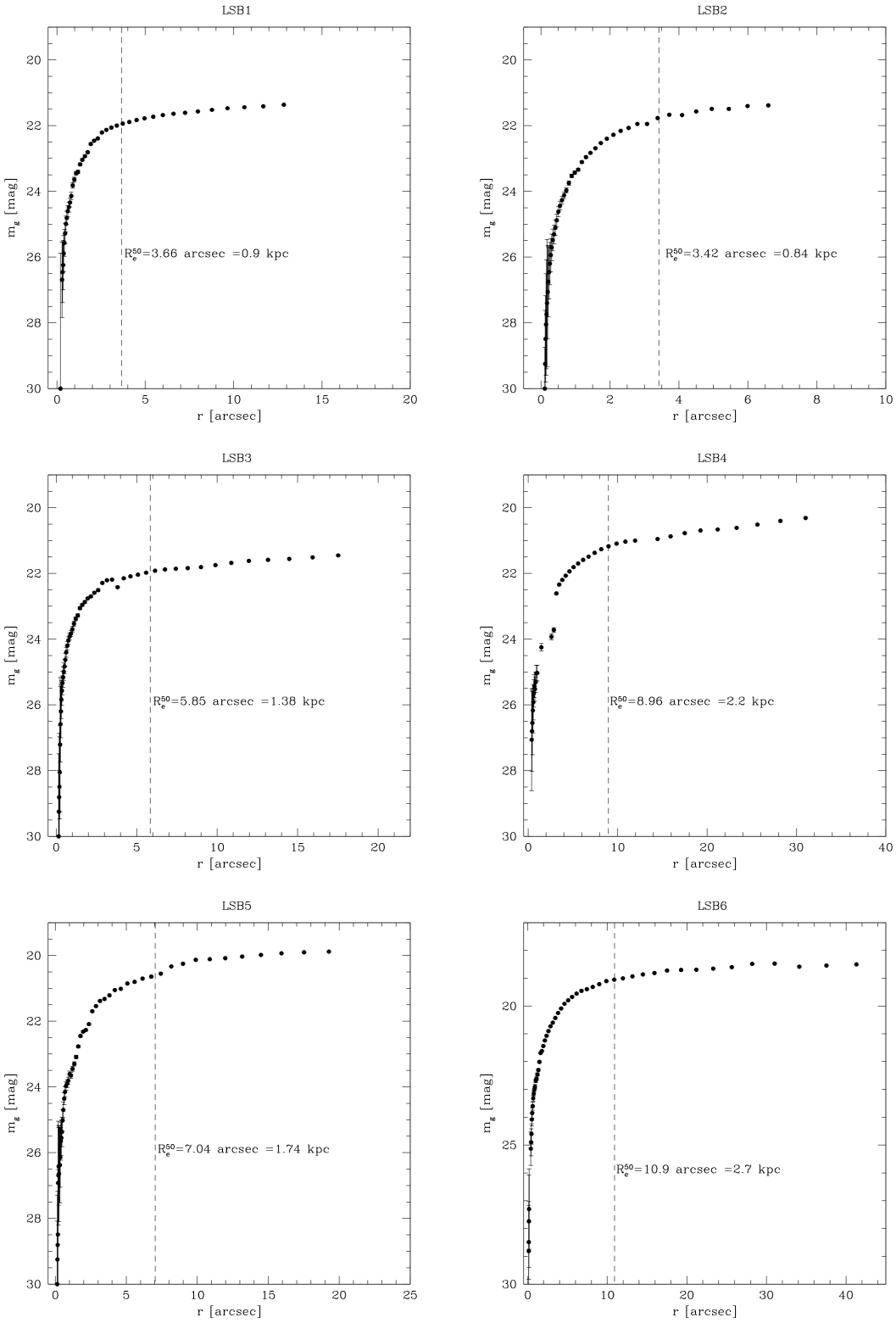

Fig. D.4. Same as Fig. C.5 for LSB 1, LSB 2, LSB 3, LSB 4, LSB 5, and LSB 6.

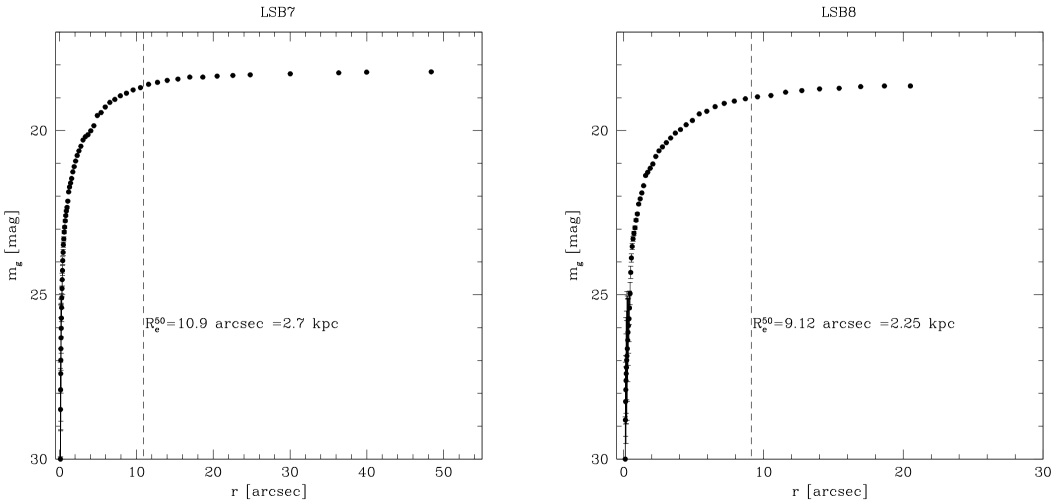

Fig. D.5. Same as Fig. C.5 for LSB 7 and LSB 8.